Deciphering the U Pb dates of sedimentary phosphates: A complex example from the Upper Cretaceous-Lower Paleogene series in northwestern Morocco

Jérémie Aubineau, Michel Séranne, Ernest Chi Fru, Marc Poujol, Radouan El Bamiki, Paul Yves Jean Antonio, Manuel Muñoz, Abdellatif Elghali, Otmane Raji, Es-Said Jourani, et al.

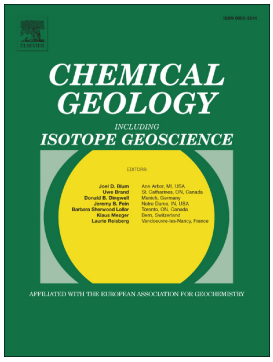

Deciphering the U-Pb dates of sedimentary phosphates: A complex example from the Upper Cretaceous-Lower Paleogene series in northwestern Morocco

Jérémie Aubineau, Michel Séranne, Ernest Chi Fru, Marc Poujol, Radouan El Bamiki, Paul Yves Jean Antonio, Manuel Muñoz, Abdellatif Elghali, Otmane Raji, Es-Said Jourani, Jean-Louis Bodinier, Fleurice Parat

PII: S0009-2541(24)00258-4

DOI: https://doi.org/10.1016/j.chemgeo.2024.122178

Reference: CHEMGE 122178

To appear in: *Chemical Geology*

Received date: 13 December 2023

Revised date: 4 April 2024

Accepted date: 16 May 2024

Please cite this article as: J. Aubineau, M. Séranne, E.C. Fru, et al., Deciphering the U-Pb dates of sedimentary phosphates: A complex example from the Upper Cretaceous-Lower Paleogene series in northwestern Morocco, *Chemical Geology* (2023), https://doi.org/10.1016/j.chemgeo.2024.122178

Deciphering the U-Pb dates of sedimentary phosphates: A complex example from the Upper Cretaceous-Lower Paleogene series in northwestern Morocco

Jérémie Aubineau[1,2]*, Michel Séranne[1], Ernest Chi Fru[3], Marc Poujol[4], Radouan El Bamiki[5], Paul Yves Jean Antonio[1,6], Manuel Muñoz[1], Abdellatif Elghali[5], Otmane Raji[5], Es-Said Jourani[5], Jean-Louis Bodinier[5] & Fleurice Parat[1]

[1]Géosciences Montpellier, Université de Montpellier, CNRS UMR 5243, Montpellier, France

[2]Géosciences Environnement Toulouse, CNRS UMR 5563 (CNRS/UPS/IRD/CNES), Université de Toulouse, Observatoire Midi-Pyrénées, Toulouse, France

[3]Center of Geobiology and Geochemistry, School of Earth and Ocean Sciences, College of Physical Sciences and Engineering, Cardiff University, Cardiff CF10 3AT Wales, UK

[4]Univ Rennes, CNRS, Géosciences Rennes, UMR 6118, 35000 Rennes, France

[5]Geology and Sustainable Mining Institute, Mohammed VI Polytechnic University, Ben Guerir, 43150, Morocco

[6]Centre for Planetary Habitability (PHAB), University of Oslo, Oslo, Norway

*corresponding author: jeremie.aubineau@get.omp.eu

Abstract

Uranium-lead geochronology rapidly generates dates of rock deposition/formation with reasonable precision and accuracy using laser ablation inductively coupled plasma mass spectrometry, which is needed for bracketing stratigraphy. However, previous radiometric U-Pb dating of biogenic (*i.e.*, bones and teeth) and sedimentary phosphate minerals have had limited success, probably because of the nanometric to micrometric crystallites that generate open system behavior. Sediment lithification inhibiting trace element exchange between minerals and porewaters and thus forcing phosphorus-rich crystallites to adopt a closed system behavior has been suggested for interpreting U-Pb dating of carbonate fluorapatite (CFA). Despite these insights, what remains lacking is extensive U-Pb CFA dating at the regional scale to test whether several processes influence the timing of U-Pb system closure by inhibiting U and Pb exchanges. Here, we report U-Pb CFA dating from four sampling sites in northwestern Morocco to understand better the meaning of U-Pb dates in CFA. The Upper Cretaceous-Lower Paleogene phosphate series yields anomalously low $^{207}Pb/^{206}Pb$ initial ratios and young dates ranging from 37.3 ± 2.4 Ma to 22.7 ± 0.7 Ma, which does not agree with the terrestrial lead model composition for Paleogene ages and the known biostratigraphic ages, respectively. We argue that ancient radiogenic Pb from leached polymetallic mineralizations of the regional environment have been incorporated into CFA and that a 25 to 40 Ma-long widespread resetting of the U-Pb system has affected the northwestern Moroccan phosphates. Neither CFA-hosted CO_3^{2-} concentrations nor rare earth element and yttrium contents indicate post-depositional modifications of the chemical nature of phosphate-bearing rocks. Burial diagenesis promoting sediment lithification is one of the mechanisms that have triggered final closure of the U-Pb system of CFA minerals and, interestingly, the sedimentation rate was probably not a controlling factor. Unexpectedly, U-Pb dates of ~23 Ma from three stratigraphic levels separated by several million years seem to be concomitant with the regional emersion and generalized continentalization of northwestern Morocco, allowing CFA to behave as a closed system. We conclude that the laser ablation inductively coupled mass spectrometry U-Pb dating of biogenic and sedimentary CFA minerals must be carefully employed to date the timing of fossilization or sediment deposition.

Keywords: U-Pb dating, carbonate fluorapatite, system closure, radiogenic Pb, Morocco

1. Introduction

Determining the precise timing of deposition of sediments that host apatite fossils (*i.e.*, bones and teeth) and sedimentary carbonate fluorapatite (CFA) minerals is critical to reconstructing the evolution of species and phosphogenesis. Modern CFA grains have typically high (>100 ppm; Arning et al., 2009) U concentrations, whereas calcitic fossils and calcite cements usually contain much lower U content (<3 ppm; Brigaud et al., 2021; Rochín-Bañaga et al., 2024). Because of the significant incorporation of U in the CFA crystal structure, laser ablation inductively coupled mass spectrometry (LA-ICP-MS) is commonly used to perform rapid and robust U-Pb dating. However, the potential use of apatite formed in sedimentary environments as a dating tool is currently challenging because the U-Pb chronometer is largely applied with limited success on both fossils and CFA minerals. Fossil teeth and CFA grains yield either U-Pb dates consistent with independent constraints but with poor precision (Balter et al., 2008; Li et al., 2023; Molnár et al., 2018; Sano et al., 2006) or radiometric U-Pb dates significantly younger than the expected ages (Aubineau et al., 2022a; Fassett et al., 2011; Greene et al., 2018; O'Sullivan et al., 2021; Rochín-Bañaga et al., 2021; Rochín-Bañaga and Davis, 2023).

Regardless of the nature of phosphate minerals, linking radiometric U-Pb apatite dates to the age of formation/deposition is not warranted. Mobility of U and radiogenic Pb has been suggested as a plausible process to explain the anomalously younger dates compared to the expected ages (Rochín-Bañaga and Davis, 2023). Also, high amounts of common Pb and low concentrations of radiogenic Pb in sedimentary apatite often hinder the ability to generate U-Pb dates with good precision and accuracy (Roberts et al., 2020). Alternatively, the application of U-Pb or Lu-Hf dating with limited success to biogenic and sedimentary apatite could be first caused by the high reactivity of the µm-sized phosphate crystallites that display a large available surface area (Herwartz et al., 2013). The small crystal size of the targeted material, coupled with high nanoscale intercrystalline porosity, are responsible for many problems, including adsorption, desorption, and diffusion, leading to continuous uptake and loss of U and Pb. Such a mechanism, in turn, would have resulted in a long-term open system behavior, resetting permanently the U-Pb radiometric system (Aubineau et al., 2022a; Greene et al., 2018). Considering the above features, closure temperature of sedimentary CFA minerals may have differed from that of igneous and metamorphic apatite. In this study, we refer to the

closure of the U-Pb system as closed system behavior at the scale of a CFA crystallite. The U-Pb system of CFA minerals may have retained an open behavior after deposition for the reasons depicted above.

It has been hypothesized that the U-Pb phosphate ages would record system closure associated with the end of CFA-porewater interactions (Aubineau et al., 2022a). Sediment lithification (i.e., transformation of sediments into solid rocks) during burial diagenesis can be viewed as an important cause for the disappearance of these interactions (Aubineau et al., 2022a; O'Sullivan et al., 2021). Yet, it remains unclear whether other mechanisms could trigger system closure of CFA minerals at the regional scale. The age of system closure – and thus processes responsible for it – after a long-term open system behavior of phosphate minerals could promote new insights into the U-Pb chronometer when applied to sedimentary environments.

Here, we explore LA-ICP-MS U-Pb dating of CFA grains from various geological settings corresponding to the Gantour tabular plateau and footwalls of the inner western High Atlas (WHA) belt in northwestern Morocco. Importantly, the Gantour plateau is not part of the Atlas system, suggesting an absence of deformation, even minimal, caused by the orogeny. We focus herein on five sampling sites of the Upper Cretaceous-Paleogene phosphate series whose geodynamic evolutions are independent (Fig. 1), one of which has already yielded two U-Pb CFA dates of 42.9 ± 1.3 Ma and 35.7 ± 2.8 Ma (Aubineau et al., 2022a). We subsequently unravel when CFA crystallites behave as a closed system in sedimentary environments. Our U-Pb CFA dating yields younger dates than expected, but these results offer a unique opportunity to study the U-Pb geochronometer at the regional scale and discuss possible geodynamic events that occurred well after phosphate deposition.

2. Geological background of Northwestern Morocco

2.1. Geodynamical framework

Morocco in Northern Africa has recorded successive orogenies through geological times, starting from the Paleoproterozoic Eburnean orogeny of the West African Craton to the Cenozoic Alpine orogeny (Michard et al., 2008). The youngest orogenic Atlas system is marked by the development of intracontinental fold belts spreading over thousands of kilometers from the Atlantic coast to Tunisia, which resulted from the movement of the African and Eurasian plates. The tectonic convergence has led

to the inversion of Mesozoic-Cenozoic subsiding rift basins through the reactivation of former syn-rift faults (Frizon de Lamotte et al., 2008; Michard et al., 2008). Consequently, the Atlas belt is characterized by a moderate shortening of ~10 and 30 km (Domènech et al., 2016; Teixell et al., 2003) and crustal root that cannot maintain isostatically the Atlas Mountains (Missenard et al., 2006, and references therein). Besides, this shortening and crustal deformation are unlikely the only factors controlling the high topography of northwestern Morocco (Babault et al., 2012; Teixell et al., 2005). Instead, an upper mantle anomaly associated with horizontal flows of the Canary mantle plume material, resulting in lithosphere thinning and/or delamination, has likely contributed to the Atlas present-day topography (Duggen et al., 2009; Missenard et al., 2008, 2006).

In Morocco, the Atlas system consists of ENE-trending High Atlas and NE-trending Middle Atlas Mountain belts (Fig. 1a). Specifically, the WHA is composed of several morpho-structural units bounded by the main thrust fronts. The inner belt – locus of the WHA's most important vertical motions – is dominated by Precambrian and Paleozoic basement rocks, whereas the North and South Atlas Front are characterized by undeformed or folded Mesozoic to Paleogene plateaus (Fig. 1b; Leprêtre et al., 2018). In addition, poorly developed foreland basins formed during the Neogene (Fig. 1b; El Bamiki et al., 2020). The Jebilet massif, located north of Marrakech, is affected by a major south-dipping reverse fault accommodating at least 4 km of shortening with about 1 km of vertical throw (Hafid et al., 2006). This clearly suggests that the North Jebilet Front (NJF) is the actual major front of the High Atlas system (Fig. 1). To the north of the NJF, the Bahira plain and Gantour basin lie outside the Atlas system and have only experienced brittle deformation during the Oligocene (Jaffal et al., 2022). They structurally form a synclinal basin owing to the vertical movement of the NJF (Saddiqi et al., 2009; Zouhri et al., 2008).

Based on low-temperature thermochronology data, Leprêtre et al. (2018) highlighted that the WHA structural blocks did not evolve similarly during the uplift phases. In connection with the Central Atlantic rifting, the pre-orogenic period is defined by the development of Triassic NW-SE oblique extension (Frizon de Lamotte et al., 2008), which promoted important thermal subsidence and, in turn, deposition of thick Mesozoic marine sequences in the vicinity of rifted areas (Ellouz et al., 2003). The thermally-induced subsidence faded away during the Late Cretaceous in response to the Eurasia-Africa convergence, which has led to the

deposition of thin Paleogene phosphate-bearing sedimentary series (Ellouz et al., 2003). Multiple phases of shortening and uplift have affected the WHA with major episodes during the Late Eocene, Oligocene-Miocene transition, and Late Miocene-Early Pliocene (Frizon de Lamotte et al., 2008, 2009; Lanari et al., 2020; Leprêtre et al., 2018; Missenard et al., 2008). In addition, Mesozoic-Paleogene sediments within the northern front of the WHA have been affected by km-scale folds (Frizon de Lamotte et al., 2008). The erosion of the WHA belt is delivering continental materials to foreland basins developed along the northern and southern fronts of the mountain (Michard et al., 2008).

2.2. Stratigraphic framework

During the Late Cretaceous to Paleogene, an intense phosphogenic event impacted the South Tethyan province, including northwestern Morocco (Pufahl and Groat, 2017; Trappe, 1998). Phosphate-rich sediments, deposited on shallow water platforms under the strong influence of Atlantic upwelling currents, are now well-preserved within vast plateaus of the western Meseta domain (e.g., Gantour, Ouled Abdoun, and Meskala basins) and along the northern and southern margins of the WHA (Fig. 1). Phosphate deposition on the Moroccan shallow shelf areas was mainly controlled by eustacy (El Bamiki et al., 2020). These phosphate-bearing sequences show variable phosphorus enrichments linked to their geographical positions regarding the phosphogenic window and post-phosphogenesis sedimentary processes (i.e., winnowing, reworking, and transport) (El Bamiki et al., 2021, 2020).

The flat-lying sediments of the Gantour basin predominantly consist of Maastrichtian limestones, marls, phosphatic sands, and yellowish clays (OCP, 1989). The overlying phosphorite horizons were deposited in a marl-dominated environment from the Cretaceous-Paleogene transition to the mid-Thanetian (Fig. 2a, Aubineau et al., 2024). Finally, *Thersitea* dolomitic limestones of Lutetian age, corresponding to a stratigraphic marker level in the Moroccan phosphate series, marked the end of the phosphogenic episode (Boujo, 1976; El Bamiki et al., 2021; Salvan, 1955). This unit is, however, significantly eroded in the Gantour plateau. Sedimentological and sequence stratigraphic frameworks are difficult to achieve because of the current industrial phosphate exploitation of the Gantour plateau.

Lateral facies changes were observed in the WHA sedimentary sequences between the shallow proximal Ouarzazate basin to the east and deeper facies of the

Souss basin (including the Erguita – ER – section) to the west (El Bamiki et al., 2020). On the other hand, the Amizmiz (AMZ), Moulay Brahim (MB), and Talentloute (TAL) sections in the central part of the WHA show little lithological variations (Fig. 2b). In this study, we sampled phosphorus-bearing rocks from Gantour, ER, MB, and TAL sites. The WHA phosphate lithofacies are genetically linked; they derive from a sedimentary differentiation of pristine phosphates by hydrodynamic winnowing, reworking, and transporting (El Bamiki et al., 2020). Consequently, thin winnowed phosphate beds accumulated in the AMZ, MB, and TAL sections, while turbiditic phosphate beds were preserved within the ER section during the interval of regional-scale maximum flooding likely near the Selandian-Thanetian transition (Fig. 2b; El Bamiki et al., 2020). Then, the area underwent a widespread regression event, as indicated by the overlying marine marls, platform carbonates, and continental sediments. Finally, the Upper Cretaceous/Paleogene sedimentary sequence of the WHA is truncated and unconformably covered by Neogene molassic sediments.

The low subsiding conditions in the western Meseta area have allowed little sediments to accumulate. As a result, phosphorites were deposited in a ~8.5 Ma time interval under an extremely low sedimentation rate of <3 m/Ma (Aubineau et al., 2024; Yans et al., 2014). In contrast, the sedimentation rate is about ten times higher in the four WHA above-mentioned sections (based on biostratigraphic data of nannoflora, El Bamiki et al., 2020).

3. Material and methods

3.1. Sampling and sample preparation

The sampling strategy is based on selectively collecting samples originating from different geological and environmental settings, as described above in northwestern Morocco’s geological history. Phosphorites from a mining well in the western Gantour Plateau (western Meseta) were collected by the OCP geologists and previously described for their mineralogical and geochemical nature (Aubineau et al., 2024, 2022b). Phosphate-bearing sediments from Moulay Brahim (31°17'36.9"N 7°59'25.3"W), Talentloute (31°31'02.7"N 7°40'24.5"W), and Erguita (30°36'50.0"N 8°54'52.6"W) sections in the WHA domain were sampled from outcrops. Dozens of kilometers separate the five sampled sites (Fig. 1b). The studied samples have been designated as DSP1 and C2M for Gantour, D-MB for Moulay Brahim, D-TAL for Talentloute, and D-ER for Erguita. In addition, published data from the Amizmiz

section (31°12'09.0"N 8°14'08.1"W) were used to complete the dataset (Aubineau et al., 2022a). Field observations and sedimentary features of the AMZ, MB, TAL, and ER sections were extensively described in El Bamiki et al. (2020).

The two Gantour phosphorites are hosted in the uppermost Maastrichtian and Upper Danian rocks (Aubineau et al., 2024). They are stratigraphically separated by ~8 m (Fig. 2a). In contrast, all selected samples of the WHA are from the correlative interval of the regional-scale maximum flooding event (Fig. 2b), which occurred during the Selandian-Thanetian transition (El Bamiki et al., 2020). For XRD analysis, each sample was crushed and milled by hand in agate mortar. For microscopic observations, trace element geochemistry, and U-Pb dating, both thin sections (Gantour samples) and polished slabs (WHA samples) were prepared using standard rock-polishing laboratory procedures at IC2MP, University of Poitiers and Geosciences Montpellier, University of Montpellier. The same specimens were analyzed for U-Pb dating and trace and rare earth element (REE) analysis.

3.2. Petrography and mineralogy

All sections, which were not carbon-coated, were examined for textural relationships under backscattered electron (BSE) mode using an FEI Quanta 200 FEG scanning electron microscope (SEM) equipped with an Oxford Instruments energy dispersive X-ray spectrometer (EDX) at MEA platform, University of Montpellier. Analytical conditions of SEM operated under a low vacuum at an accelerating voltage of 15 kV, 1 nA beam current, and a working distance of 10 mm.

X-ray diffraction (XRD) mineral analyses were done on powdered bulk samples to characterize the mineralogy of Gantour, MB, TAL, and ER phosphate-bearing rocks. XRD diffractograms were acquired with a Bruker D8 ADVANCE diffractometer (CuKα radiation) operating at 40 kV and 40 mA at RRXG platform, University of Montpellier. Analysis of bulk powders was performed over an angular range of 5–62° 2θ and a step size of 0.02° 2θ per 2 s. Bruker Eva software was used for indexing peaks, and XRD patterns were compared with reference data (Brindley and Brown, 1980). In addition, the semi-quantification of bulk mineralogy was achieved through the Rietveld refinement of XRD patterns using the Profex 4.3.1 interface with the program BGMN (Döebelin and Kleeberg, 2015).

3.3. Trace and REE analysis

Trace element concentrations (Y, REE, U, Th, and Pb) were measured by LA-ICP-MS using a ThermoFinnigan Element XR ICP-MS coupled to a Geolas platform housing a 193 nm Compex 102 laser from LambdaPhysik at AETE platform (OSU-OREME), University of Montpellier. Gantour, MB, and TAL samples were carefully analyzed to screen any possible weathering and diagenetic influences. Erguita samples were not investigated because of the limited presence of phosphate grains. Measurements were performed with a pulsed 6 Hz laser beam of 6 $J.cm^{-2}$ energy density and 50 µm spot size. LA-ICP-MS analyses began with a preablation pulse of 1 s using a spot size of 65 µm. Then, every signal was collected, including 70 s blank and 40 s ablation. LA-ICP-MS measurements were calibrated with NIST standard reference material 612 (Pearce et al., 1997), while BIR-1G standard was analyzed as unknown. LA-ICP-MS standard values and their corresponding standard error and detection limits are presented in Table S1. The relative standard deviation values (RSD in % = standard deviation / mean x 100) for all trace elements of BIR-1G were between 0.8–27.5%. The average deviation of the measured BIR-1G concentrations from the reference values (Geo-REM database; http://georem.mpch-mainz.gwdg.de) was <4.5% (ranging from 0.2% to 18.2%). Data reduction was done using Glitter software (Griffin, 2008). We chose a uniform CaO concentration of 54 wt.% as the internal standard value, which best reflects the composition of this material (Aubineau et al., 2022b). Time-resolved spectra were checked for accuracy by removing mixed signals in the analyzed volumes. When elemental concentrations were lower than the sum of the detection limit and standard error, values were discarded.

The REE and yttrium (REEY) values have been normalized to the Post-Archean Australian Shale (PAAS; Taylor and McLennan, 1985), a widely used standard for normalizing geochemical data from sedimentary rocks. This method promotes comparisons with other studies. Similarly to the REEY systematics described in Aubineau et al. (2022a), Ce, Pr, Gd, and Y anomalies were calculated to assess the REEY behavior during formation and post-depositional conditions (Bau and Dulski, 1996; Planavsky et al., 2010; Shields and Stille, 2001). Finally, boxplots provide a concise visualization of the REE distribution within phosphorites using the R version 3.5.1.

3.4. U-Pb analyses

U-Pb geochronology on sedimentary apatite, i.e. carbonate fluorapatite, was undertaken on the Gantour and WHA (MB, TAL, and ER) phosphate-bearing rocks. Thirty to 54 different CFA grains of varying grain size (40 – 800 µm) were analyzed per sample. No more than two analyses per CFA grain were performed. In this study, we have targeted CFA peloids (described in the next section) rather than phosphatized bone fragments or coprolites.

Similarly to the AMZ samples (Aubineau et al., 2022a), *in situ* U-Pb dating was conducted at the GeOHeLiS analytical platform, University of Rennes, using a quadrupole Agilent 7700x ICP-MS and an ESI NWR193UC Excimer laser. The instrumental conditions, analytical set-up, and data reduction are reported in Table S2. The Madagascar apatite standard was used as the primary apatite reference material (Chew et al., 2014 ; 473.5 ± 0.7 Ma), while Durango apatite standard (McDowell et al., 2005 ; 31.4 ± 0.2 Ma) was treated as unknown to control reproducibility. Durango yielded U-Pb ages of 30.9 ± 1.1 Ma (n = 40), 32.7 ± 1.1 Ma (n = 16), and 32.0 ± 1.5 Ma (n = 17) in three different batches between September 2021 and April 2023 (Fig. S1). U-Pb isotopic data of standards, at 2 standard error confidence, are reported in Table S3. U-Pb phosphate dating was plotted in Terra-Wasserburg diagrams using IsoplotR (Vermeesch, 2018).

4. Results

4.1. Mineralogical and petrographic characterization

XRD mineralogical data show that the diffraction peaks in the 2.79 to 2.69 Å region reveal the presence of CFA as the main phosphate mineral in all Moroccan sedimentary phosphate rocks (Fig. S2a). The estimated CO_3^{2-} content of CFA in the studied samples is higher than 4.7 wt.% (Table 1), which matches with the known CFA-hosted CO_3^{2-} concentrations in Moroccan phosphorites (Aubineau et al., 2022a, 2022b; Cosmidis et al., 2013; El Bamiki et al., 2023; Kocsis et al., 2014; Nguidi et al., 2021). XRD data also reveal that the ER rocks mainly comprise quartz and dolomite with only trace amounts of calcite and CFA (Fig. S2), consistent with the turbiditic depositional environment (El Bamiki et al., 2020). In contrast, the Gantour, AMZ, MB, and TAL samples are dominated by CFA with heterogeneous quartz and carbonate contents (Fig. S2, Aubineau et al., 2024, 2022a, 2022b; El Bamiki et al., 2023). Moreover, clay minerals are of varying compositions and proportions. The latter are

characterized by smectite, sepiolite, palygorskite, and detrital illite/mica to a lesser extent. Both sepiolite and palygorskite typically form from supersaturated conditions that are usually found in lacustrine and lagoonal environments under semi-arid/arid and evaporitic climatic conditions (Singer and Galan, 1984).

The studied Moroccan rocks host unsorted, dark brown phosphatic grains known as peloids that show a spheroidal to elliptical shape (Fig. 3a). Under SEM, the phosphatic peloids are densely packed (except at ER site) and consist of rounded and structureless particles of varying grain size (Fig. 3b-l). The average grain size of the studied Gantour CFA peloids is 180 ± 86 µm (1 standard deviation, n = 70) (Fig. 3b, c). The Gantour phosphorites are also composed of phosphatized bioclasts and coated phosphate grains, comprising distinct concentric zonation of CFA layers (Fig. 3b, c). This feature would indicate changes in the hydraulic regime during phosphogenesis (Pufahl and Grimm, 2003). In the northern WHA fronts (AMZ, MB, and TAL), the CFA peloids are larger, with an average grain size of 314 ± 149 µm (1 standard deviation, n = 112) (Fig. 3d-i). The proportion of CFA peloids at ER is lower than other sites, and the grain size of CFA is the smallest of the dataset with a mean of 135 ± 47 µm (1 standard deviation, n = 35) (Fig. 3j-l). The fine-grained CFA peloids at ER site are likely derived from the pristine phosphatic lithofacies that have been transported basinward (El Bamiki et al., 2020), while the larger phosphatic grains from Gantour, AMZ, MB, and TAL sites support deposition landward close to the phosphogenesis window after repetitive wave and storm winnowing (El Bamiki et al., 2020; Pufahl and Groat, 2017). Finally, all particles are embedded in a carbonate cement or clay matrix with varying proportions of detrital grains.

4.2. Rare earth element and yttrium (REEY) geochemistry

LA-ICP-MS REEY results are provided in Table S4. Our data show a slight heterogeneity in REE concentrations between the Gantour and WHA phosphorites (Fig. 4a). In detail, Gantour, AMZ, MB, and TAL samples yield mean REE concentrations between 119–215 ± 22–41 ppm (n = 7), 109–186 ± 38–76 ppm (n = 40; Aubineau et al., 2022a), 89–125 ± 36–59 ppm (n = 50), and 108–110 ± 32–55 ppm (n = 50), respectively.

The PAAS-normalized REEY ($REEY_{SN}$, where SN represents values normalized to PAAS) patterns of WHA phosphorites are quite similar to each other, while those of Gantour phosphorites stand out clearly with higher HREE abundances

(Fig. 4b). All $REEY_{SN}$ patterns yield features akin to those of modern seawater, including LREE depletions relative to HREE, negative Ce anomalies (more pronounced in Gantour samples), positive Gd anomalies, and Y enrichments (Alibo and Nozaki, 1999; Bau et al., 1997; Bau and Dulski, 1996; De Baar et al., 1985). The absence of MREE enrichment is also a specific characteristic of modern seawater, as demonstrated by the $(Sm/Yb)_{SN}$ and $(Sm/Pr)_{SN}$ ratios that unambiguously plot on the HREE enriched field for all studied phosphorites (Fig. 5a). In detail, the Gantour and WHA samples show slight Gd enrichments; the $(Gd/Gd^*)_{SN}$ values range from 1.12 to 1.44 (n = 107) (Table S4). The average Y/Ho ratios are high in all phosphorites (>52 in MB and TAL samples, >48 in Gantour samples; Table S4). On the $(Ce/Ce^*)_{SN}$ and $(Pr/Pr^*)_{SN}$ plot, phosphorites fall within field IIIb, corresponding to a true negative Ce anomaly (Fig. 5b). Moreover, enrichments of LREE with respect to MREE and HREE can be illustrated across the $(La/Yb)_{SN}$ and $(La/Sm)_{SN}$ plot (Fig. 5c). Most of the mean $(La/Yb)_{SN}$ ratios fall outside the range of modern seawater, while mean $(La/Sm)_{SN}$ values are comparable to those of modern seawater. This pattern suggests preferential adsorption of LREE onto surface crystallite (Reynard et al., 1999). Through coeval enrichments of La and Y, weathering and diagenesis may be highlighted using the $(Y/Y^*)_{SN}$ and $(La/Nd)_{SN}$ plot (Shields and Stille, 2001). This is not the case for the Moroccan phosphorites, which fall mainly within the seawater field (Fig. 5d).

4.3. U-Pb CFA dating

Our U-Pb LA-ICP-MS data, at 2 standard errors, are reported in Table S5. We have analyzed over 30 different CFA grains of various sizes within each phosphate-bearing rock at Gantour, MB, TAL, and ER sites. Where possible, the core and edge of CFA grains were analyzed. The WHA phosphatic peloids exhibit appreciable amount of U, ranging from 20 to 67 ppm (n = 140) (not measured in Gantour and ER samples) (Table S4) (Aubineau et al., 2022a). Uranium concentrations of teeth and coprolites in the Gantour basin range from 7 to 335 ppm (Kocsis et al., 2016). Although our investigated material differs, we consider that the Gantour CFA peloids have similar U concentrations since coprolites phosphatized in the vicinity of CFA formation (Cosmidis et al., 2013).

The U-Pb isotopic measurements are discordant with $^{207}Pb/^{206}Pb$ ratios varying between 0.34–0.44, 0.56–0.73, 0.67–0.75, and 0.41–0.80 for Gantour, MB,

TAL, and ER samples, respectively (Fig. 6). Interestingly, the absolute values of the $(^{207}Pb/^{206}Pb)_0$ are substantially lower than the ~60 Ma-old crustal average of about 0.839 predicted by the Stacey and Kramers model (Fig. 6; Stacey and Kramers, 1975). The CFA grains spreading considerably outside of error along the mixing line between common Pb and radiogenic Pb were excluded from their regressions. We hypothesize that a substantial gain of U, Pb loss or the heterogeneous nature of CFA grains in terms of texture and geochemical compositions (Aubineau et al., 2022b, 2022b) could have generated excess scatter (Roberts et al., 2020).

The Gantour phosphorites from two distinct stratigraphic strata (~62 and ~66 Ma) yield equivalent U-Pb CFA dates of 23.9 ± 1.4 Ma (MSWD = 2.2, n = 27) and 23.6 ± 2.1 Ma (MSWD = 2.3, n = 23) (Fig. 6a). The upper intercept was anchored through the initial Pb isotopic composition using the Stacey and Kramers model. The anchored Tera–Wasserburg lower intercept dates of 68.3 ± 9.0 Ma (MSWD = 250) and 64.4 ± 6.0 Ma (MSWD = 110) are by far the most imprecise dates (Fig. 6a). In the southern front of the WHA, the ~59 Ma-old ER phosphate-bearing samples from the maximum flooding interval yield a U-Pb CFA date of 22.7 ± 0.7 Ma (MSWD = 2.4, n = 58) (Fig. 6b). The anchored Tera–Wasserburg lower intercept date of 27.0 ± 1.5 Ma (MSWD = 15) falls well outside the uncertainty limits on the assumed age (Fig. 6b). The interval of maximum bathymetry was also prospected in the northern front of the WHA domain for U-Pb geochronology. For both ~59 Ma-old MB and TAL samples, U-Pb CFA dating defines lower intercepts of unanchored discordia dates of 33.8 ± 1.9 Ma (MSWD = 2.0, n = 87) and 37.3 ± 2.4 Ma (MSWD = 1.7, n = 106), respectively (Fig. 6c), which is consistent with the U-Pb CFA date of 35.7 ± 2.8 Ma reported in AMZ13 (Fig. 6c; Aubineau et al., 2022a). If the discordias are anchored to a $^{207}Pb/^{206}Pb$ value of 0.839 (Fig. 6c), the resulting lower intercept dates are 49.5 ± 2.4 Ma (MSWD = 7.5) and 55.7 ± 2.3 Ma (MSWD = 5.5) for MB and TAL samples, respectively. Besides, the lower part of the maximum flooding interval in Amizmiz previously yielded a U-Pb CFA date of 42.9 ± 1.3 Ma (MSWD = 2.3) (Fig. 6c; Aubineau et al., 2022a). Overall, the upper part of the maximum flooding zone in the northern front of the WHA (AMZ13, MB, and TAL samples) corresponds to a mean date of 35.3 ± 0.4 Ma. The unanchored dates were preferred since anchored discordias show excess scatter (i.e., high to extremely high MSWD). The MSWD of the unanchored discordias as a function of the sample size may be slightly higher

than the acceptable range (Spencer et al., 2016; Wendt and Carl, 1991), but this could be due to the presence of other U-bearing minerals within the ablated material such as phyllosilicates (Aubineau et al., 2022a), increasing the data point uncertainties.

In light of these considerations, our U-Pb isotopic data from several Moroccan sites show three distinct U-Pb dates for a single stratigraphic interval (i.e., maximum flooding zone) and a concomitant U-Pb date (i.e., ~23 Ma) within three distinct stratigraphic strata (Fig. 7). Despite the apparent robustness of isochrons (MSWD < 2.4), all U-Pb dates are younger than the known expected ages by ~25 or ~40 Ma.

5. Discussion

5.1. Origin of the CFA elemental compositions

With time, weathering and diagenetic processes may promote rapid decarbonation of CFA crystallites (McClellan and Van Kauwenbergh, 1991). However, the extent of CO_3^{2-} incorporation in CFA is firstly controlled by the equilibrium with seawater or interstitial waters immediately below the water-sediment interface during phosphogenesis (Nathan, 1984). This equilibrium yields CFA-hosted CO_3^{2-} concentrations between 3 to 8 wt.% (Compton and Bergh, 2016; Nathan, 1984), implying that our studied CFA crystallites in the Gantour and WHA phosphate-bearing rocks are likely unaltered (the lowest CO_3^{2-} concentration is 4.7 $\pm$ 0.5 wt.%, n = 12). Specifically, the biological activity in the sediment determines the dissolved CO_3^{2-}-saturated fluids in porewaters (Glenn et al., 1988). Fluctuating rates of organic matter remineralization by heterotrophs imply changes in porewater alkalinity, controlling the degree of substitution of CO_3^{2-} for PO_4^{3-} between the CFA crystallites and porewaters. Thus, this process would explain the heterogenous CFA-hosted CO_3^{2-} concentrations ranging from 4.7 to 9.3 wt.% (Table 1) in the Moroccan phosphate-bearing rocks.

The REEY enrichment in sedimentary phosphate minerals offers the opportunity of evaluating the seawater and porewater chemistry of depositional environments and/or post-depositional changes such as transportation and redeposition, diagenesis, and weathering (e.g., Aubineau et al., 2022a; El Bamiki et al., 2023; Lumiste et al., 2019; Reynard et al., 1999; Shields and Stille, 2001; Yang et al., 2021). Trace element CFA composition provides significant evidence for seawater as a common source of REEY for CFA in the Gantour and WHA

phosphorites. This interpretation also agrees with REE_{SN} patterns of fossil bioapatite (n > 200) from the Moroccan Ouled Abdoun and Gantour basins (Kocsis et al., 2021, 2016). Although the REE abundance of fossil bioapatite and CFA peloids may vary each other, there is no significative fractionation of REE between the different types of phosphatic material, which promotes comparisons.

Quantitative incorporation without fractionation may explain the REE enrichment factor of 10^6 to 10^7 in the Moroccan studied CFA compared to seawater (Reynard et al., 1999). Nonetheless, an average $(La/Yb)_{SN}$ ratio of 0.8 ± 0.1 (n = 107, Table S4) compared to 0.2-0.5 for the seawater (Reynard et al., 1999) in the Moroccan CFA indicates the occurrence of fractionation of REE between CFA and seawater. Controlled by CFA crystal surface chemistry, LREEs preferentially accumulate compared to HREEs in phosphates via adsorption during 'early'/weak diagenesis (Koeppenkastrop and De Carlo, 1992; Reynard et al., 1999). In contrast, 'late'/extensive diagenetic recrystallization promotes the enrichment of MREE with respect to LREE and HREE ($(La/Sm)_{SN} < 0.3$) via substitution mechanisms (i.e., MREE arching, (Reynard et al., 1999). In addition, anoxic porewater conditions resulting in the reduction of REE-rich Fe-oxides can also lead to a MREE bulge pattern (Haley et al., 2004), which is not observed in the Moroccan CFA. Taking this into consideration, our dataset points to surface adsorption as the dominant REE enrichment mechanism onto the CFA grains. Moreover, exposure and meteoritic weathering theoretically involve preferential retention of La, Gd, and Y, resulting from their specific electronic configurations (Shields and Stille, 2001). Our results, with average $(Y/Y^*)_{SN}$ and $(La/Nd)_{SN}$ ratios of 2.1 ± 0.2 and 1.4 ± 0.1 (n = 107; Table S4), respectively, compared to 2.1 ± 0.4 and 1.5 ± 0.4, respectively, for the unaltered and recent Namibian phosphorites (Lumiste et al., 2019), indicate that phosphate weathering did not favor the accumulation of the more stable lanthanides in our samples. Furthermore, Ce_{SN} depletions across the studied samples point to a Ce uptake from oxic-suboxic seawater or porewaters. These redox conditions were likely more pronounced in the Gantour Plateau. Thus, the Moroccan shallow platform on the eastern passive margin of the central Atlantic Ocean was globally well-oxygenated at the time of REEY uptake by phosphate minerals.

In light of the above considerations, elevated concentrations of CFA-hosted CO_3^{2-} are indicative of unaltered phosphatic grains. The marine chemical

environment of the northwestern Moroccan shallow platform reflects near-pristine seawater-like signature as indicated by the specific REE patterns within CFA minerals. However, REEY uptake in bioapatite and CFA may occur over dozens of millions of years (Aubineau et al., 2022a; Greene et al., 2018; Herwartz et al., 2013, 2011; Kocsis et al., 2010). Thus, the prediction of the exact seawater conditions under which CFA grains initially formed is beyond our knowledge. The data, however, hint that the REEY composition of CFA is controlled by seawater-dominated pore fluids rather than post-depositional processes. Importantly, the adsorption mechanism of LREE with respect to HREE would have preferentially occurred during the 'early'/weak diagenesis, which is not surprising due to the high reactivity of the µm-size phosphatic crystallites (e.g., (Aubineau et al., 2022b; Mänd et al., 2018). Finally, transformations of phyllosilicates during 'late'/extensive diagenesis or fluid flows associated with post-depositional tectonic activity are not supported by the available evidence (i.e., presence of smectite and detrital clay minerals and absence of illite/smectite mixed-layer minerals or other clay minerals that derive from diagenetic fluid-rock interactions).

5.2. U-Pb systematics

At first glance, our new U-Pb CFA dating give dates inconsistent with the independent geological constraints. They also testify that the U and Pb compositions of CFA minerals do not reflect the composition at the CFA formation (i.e., not primary), as opposed to that of CO_3^{2-}. Nevertheless, U-Pb dates much younger than stratigraphic age are being increasingly reported by LA-ICP-MS U-Pb dating of both fossil bioapatite and CFA peloids (Aubineau et al., 2022a; Greene et al., 2018; Rochín-Bañaga et al., 2021; Rochín-Bañaga and Davis, 2023).

The nature and grain size of the studied Moroccan phosphatic lithofacies bears evidence of winnowing, reworking, and transport of primary phosphates (El Bamiki et al., 2020). The intensity of these sedimentary processes, together with the proximity of a detrital source (at ER site, for example), have controlled the degree of P enrichment of phosphatic sediments (El Bamiki et al., 2023). Despite repeated hydrodynamically-driven winnowing and reworking processes, CFA resisted chemical changes and preserved its original geochemical signature (El Bamiki et al., 2023). The grain size of CFA peloids significantly differs from Erguita and Gantour sites (Fig. 3), which indicates that a relationship between the U-Pb CFA dating and grain size is

unlikely. The Moroccan CFA peloids are composed of densely-packed micrometric crystallites that show rod-shaped and sphere-like morphologies with no significant variations of crystallite size (Aubineau et al., 2022b, 2022a; El Bamiki et al., 2023). High carbonate content within the fluorapatite structure implies a reduction of crystallinity (LeGeros et al., 1967), suggesting that CFA at ER site have a higher degree of crystallinity (CO_3^{2-} content: 4.7–5.4 wt.%) than other sites (CO_3^{2-} content: > 7.1 wt.%). Yet, the Gantour and ER CFA peloids yield similar U-Pb dates, which hints that the CFA crystallinity does not explain the variations of the U-Pb dates and $^{207}Pb/^{206}Pb$ ratios. Besides, sedimentary apatite minerals rapidly form as little as a few years after nucleation (Burnett et al., 1988), suggesting limited differences of $^{207}Pb/^{206}Pb$ and $^{238}U/^{206}Pb$ ratios between the core and edge of phosphatic peloids. We did not observe two or more discordias at the sample scale, which implies a unique event responsible for the observed isochrons. Combined, the U-Pb CFA dates are not sample-, grain- or crystallite-dependent.

Although the Moroccan CFA peloids have low amounts of radiogenic Pb, the data define a single linear array with a large spread in U/Pb ratios and relatively low uncertainties. The mobility of U and radiogenic Pb without a total reset of the U-Pb chronometer would not result in well-defined isochrons (Roberts et al., 2020). On the other hand, the upper intercepts ($^{207}Pb/^{206}Pb$ initial values) substantially deviate from the expected ~60 Ma-old terrestrial Pb composition.

A total reset of the U-Pb chronometer in CFA after deposition in the Paleogene would have resulted in a counter-clockwise rotation of the isochron, leading to younger U-Pb dates. The latter proposition is difficult to ascertain, however Y speciation in CFA minerals could provide insights into sorption model for U (Bonnet et al., 2023). Using X-Ray absorption spectroscopy, substitution of Y for Ca(2) site, together with Y adsorption, are likely mechanisms for explaining the incorporation of divalent cations in sedimentary phosphate minerals (Bonnet et al., 2023). Uranium and Pb also substitute for Ca in natural CFA (Luo et al., 2009; Pan and Fleet, 2002), but the lack of knowledge of the U and Pb speciations in such minerals severely hampers the understanding of the U-Pb dating at the scale of a CFA crystallite. Considering that U, Pb, and Y may have comparable speciation, adsorption/desorption mechanisms would facilitate U and Pb mobility in CFA during low-temperature CFA-porewater interactions. Nonetheless, if new uptake of U and common Pb occurred at intermediate Paleogene times, the $^{207}Pb/^{206}Pb$ initial ratios

should be around 0.84 as predicted by the terrestrial Pb model (Stacey and Kramers, 1975), which still does not explain the observed low $^{207}Pb/^{206}Pb$ initial ratios unless CFA peloids have incorporated unsupported radiogenic Pb from the local environment. Then, the phosphatic grains would have reequilibrated from a more radiogenic Pb source than the $^{207}Pb/^{206}Pb$ composition predicted by the terrestrial lead model in the Cenozoic (Stacey and Kramers, 1975). In other words, the CFA peloids would have partially inherited the radiogenic Pb signature of an ancient source whose uranium decay would have produced Pb in a closed system for a long time. This might be expected as CFA are not igneous apatites that are derived from a fractionation process.

This Pb inheritance from an older source is not an isolated phenomenon and arises from the leaching of U-bearing minerals near the depositional settings (Roberts et al., 2020). Polymetallic mineralizations containing radiogenic Pb and formed from the Neoproterozoic-Cambrian transition to the Permian are a widespread feature across Morocco (Gasquet et al., 2005; Lotfi et al., 2008; Rossi et al., 2016). Considering the above potential source rocks of leached radiogenic Pb and the Moroccan paleogeography in the Paleogene (Boujo, 1976; El Bamiki et al., 2021, 2020), the Anti-Atlas and Jebilet Massif could have fed the WHA (AMZ, MB, TAL, and ER) and Gantour samples, respectively. These source rocks, combined with the incorporation of both common and radiogenic Pb into CFA crystallites in varying proportions when they reequilibrated, provide a reasonable explanation of the low and heterogeneous $^{207}Pb/^{206}Pb$ initial ratios (0.481-0.486 at Gantour and 0.750-0.788 in the WHA).

5.3. Significance of U-Pb dates in sedimentary CFA peloids

Our data produce fairly robust isochrons (MSWD <2.4) with lower intercept dates 42.9, 34.5, and ~23 Ma from three distinct geographical areas (this study and Aubineau et al., 2022a), suggesting that several episodes both locally and regionally would have controlled the sedimentary apatite U-Pb system. The latter proposition could not have been highlighted by Aubineau et al. (2022a) since they only focused on a single geological site (Amizmiz section), which demonstrates the importance of studying several sections at the regional scale. We propose that the long-term open system behavior of CFA, possibly resulting from the high crystallite reactivity and crystallographic position of U and Pb, would have generated extensive elemental

exchanges at the atomic scale, favoring a continuous reset of the U-Pb radiometric system (Aubineau et al., 2022a; Greene et al., 2018; Herwartz et al., 2013, 2011; Kocsis et al., 2010). This phenomenon likely lasted until the interactions between CFA crystallites and pore fluids ended. Furthermore, CFA grains provide important clues on the fluid composition in Pb of the local environment. A further question is whether the interruption of these interactions integrates into the northwestern Morocco's geological history.

The timing of U-Pb system closure would have been contemporary in CFA from the Gantour Plateau and the southern front of the WHA belt. Meanwhile, the range of U-Pb system closure of all WHA samples is heterogeneous despite belonging to the same stratigraphic interval. To reconcile our contrasting U-Pb dates, we propose a conceptual reconstruction of the studied phosphate-bearing sedimentary sequences that underwent successive phases of subsidence and uplift during the Cenozoic (Fig. 8, see the geological background for details). The diverging evolution of thermal subsidence between the Gantour Plateau and the northern and southern fronts of the WHA during the Triassic to Mid-Paleogene accounts for thickness variations of sedimentary sequences (Charton et al., 2021; Ellouz et al., 2003; Jaffal et al., 2022; Michard et al., 2008). In the WHA (AMZ, MB, TAL, and ER sites), deposition of P-bearing rocks occurred at the Selandian-Thanetian transition and, later, gave way to P-poor shallow marine sedimentation (Fig. 8a, b; El Bamiki et al., 2020). In the Gantour basin, the two studied horizons were deposited during the late Maastrichtian and late Danian (Fig. 8c; Aubineau et al., 2024), which are, therefore, >3 Ma older than the WHA P-bearing rocks.

In the northern front of the WHA (AMZ, MB, and TAL sites), the U-Pb CFA chronometer recorded closure of the U-Pb system between the Late Eocene and Oligocene-Eocene transition (Fig. 8a). This pattern could be related to progressive lithification during burial diagenesis, as suggested by Aubineau et al. (2022a). It is reasonable to assume that the sedimentation rate would have impacted continuous burial until lithification. Meanwhile, in the southern front of the WHA (ER section), CFA particles yield an Oligo-Miocene U-Pb date (Fig. 8b). It means that CFA grains still behaved as an open system during the Oligocene-Eocene transition. Thus, the proposition supporting that sedimentation rate could have somehow contributed to locking the U-Pb system is not verified. The sedimentation rate at Erguita is equivalent to or higher than that of the AMZ area (El Bamiki et al., 2020).

Consequently, another closure mechanism is required to explain the lack of age unity. With the available dataset, we are unable to explain the weakness of sediment lithification on the U-Pb geochronometer at Erguita. According to our findings, lithification is not related in a straightforward way to sedimentation rate. Surprisingly, U-Pb dates in Gantour phosphorites indicate that CFA also behaved as a closed system at the Oligocene-Miocene transition (Fig. 8c), implying that a unique regional-scale event affected several Moroccan areas.

Inversion of the Atlas basin interrupted the subsidence evolution of the Moroccan phosphate basins. Based on low-temperature thermochronology, the first upfit phase restricted to the inner units of the High Atlas belt may have started in the Late Eocene (Leprêtre et al., 2018; Missenard et al., 2008). At the same time, in the northern flank of the WHA, phosphorites had already been lithified during burial. The High Atlas realm was rapidly exhumed in the wake of the earliest Miocene (Fig. 8a, b; (Balestrieri et al., 2009; Leprêtre et al., 2018). To explain the lack of isotopic modifications of the lithified phosphorites at AMZ, TAL, and MB sites during uplift, we presume that hydrothermal circulations linked to tectonic activity and heating of the sediment pile were insignificant to (i) reset the U-Pb system of CFA minerals and (ii) change the clay mineralogy, CFA-hosted CO_3^{2-} composition, and REEY distribution of phosphatic grains in the northern flank of the WHA. The main crustal vertical movements in the early Miocene were still restricted to the inner WHA belt (Frizon de Lamotte et al., 2009). On the other hand, the earliest Miocene uplift could have favored closure of the U-Pb system by inhibiting CFA-porewater interactions in the ER rocks. The presence of different structural units in the WHA belt, evolving independently (Leprêtre et al., 2018), could justify why the U-Pb isotope system of CFA minerals remained open up during burial in the southern flank of the WHA, whereas it closed in the northern flank of the WHA.

The significance of the Oligo-Miocene uplift event could probably be explained by the occurrence of a hot mantle anomaly (also called Moroccan Hot Line) since the Early Miocene, resulting in relief building (Babault et al., 2012; Duggen et al., 2009; Missenard et al., 2006; Teixell et al., 2005). Consequently, transforming the depositional conditions from marine to non-marine would have effectively inhibited CFA-porewater interactions within the WHA realm (ER site) and beyond (Gantour Plateau). We are not advocating that the U-Pb CFA ages record the establishment of the Moroccan Hot Line and related uplift. Instead, and considering the entire

geochemical dataset and age discrepancies, we hypothesize that closure of the U-Pb system in the Gantour and Erguita CFA likely resulted from an uplift-related event that resulted in continentalization of northwestern Morocco at the Oligocene-Miocene transition (Fig. 8b, c). A final uplift pulse in the High Atlas belt during the Late Miocene-Early Pliocene, together with the thermal anomaly beneath the northwest African plate, produced the present-day topography in northwestern Morocco (Fig. 8; Duggen et al., 2009; Frizon de Lamotte et al., 2009; Lanari et al., 2020; Leprêtre et al., 2018; Missenard et al., 2006).

6. Conclusion

LA-ICP-MS U-Pb dating of sedimentary apatite minerals is highly challenging to date the timing of deposition. We have used REEY- and CO_3^{2-}-based proxies to show that CFA minerals in the phosphate-bearing sedimentary sequences of Morocco were barely affected by post-depositional alterations assumed to be the most common cause of open-system behavior. Nonetheless, it is indisputable that the $^{207}Pb/^{206}Pb$ and $^{238}U/^{206}Pb$ ratios are not related to what would be expected during CFA formation. In addition, CFA has incorporated unsupported radiogenic lead derived from the local environments probably during reequilibration of the crystallites.

Our new results show that two mechanisms, i.e. burial diagenesis and continental emersion linked to uplift, resulted in final closure of the U-Pb system of µm-sized CFA crystallites, which occurred 25 and 40 Ma after sediment deposition. Regardless of the invoked mechanism, fluid-rock interactions ceased and would have forced the U-Pb geochronometer to behave as a closed system. Therefore, dating CFA material that has remained a closed isotopic system since its formation is increasingly difficult. Importantly, we highlight that both local and regional geological episodes likely controlled the U-Pb system of the sedimentary phosphate minerals.

This study demonstrates that U-Pb CFA dates may not provide precise timing for phosphogenesis, fossilization, and REEY mineralization, but that if well constrained, valuable insights can be gained on the geological mechanisms that drove system closure. These findings are important because they show that even the Gantour CFA, being beyond the WHA realm, does not accurately record the depositional U-Pb ages of the phosphate-bearing rocks. Consequently, multiple lines of evidence are advocated for assessing whether teeth, bones, and sedimentary CFA retain a primary signal.

Acknowledgments

This work was funded by the University of Montpellier (UM), University of Mohammed VI Polytechnic (UM6P), and *Office Chérifien des Phosphates* (OCP) S.A. [UM-UM6P specific agreement n°190775 relating to the UM6P-UM/CNRS framework agreement n°190759; OCP-UM6P specific agreement n° 7 “Multi-scale distribution of minor and trace elements in Moroccan phosphate deposits” relating to the OCP-UM6P framework agreement in Sciences & Technology]. In particular, Jamal Amalik, OCP Innovation, is deeply thanked for his vital involvement in the scientific projects between OCP, UM6P, and UM. We are grateful to Claude Laforest (University of Poitiers), Doriane Delmas (UM), and Christophe Nevado (UM) for the preparation of high-quality thin sections and polished slabs. Also, Bernard Fraisse, Olivier Bruguier, and Frédéric Fernandez are thanked for their technical assistance during analytical works performed at, respectively, RRXG, AETE, and MEA platforms of UM. Finally, we warmly acknowledge the scientific board of Geoscience Montpellier for their support in 2022 and 2023.

References

Alibo, D.S., Nozaki, Y., 1999. Rare earth elements in seawater: particle association, shale-normalization, and Ce oxidation. Geochimica et Cosmochimica Acta 63, 363–372. https://doi.org/10.1016/S0016-7037(98)00279-8

Arning, E.T., Lückge, A., Breuer, C., Gussone, N., Birgel, D., Peckmann, J., 2009. Genesis of phosphorite crusts off Peru. Marine Geology 262, 68–81. https://doi.org/10.1016/j.margeo.2009.03.006

Aubineau, J., Parat, F., Chi Fru, E., El Bamiki, R., Mauguin, O., Baron, F., Poujol, M., Séranne, M., 2022a. Geodynamic seawater-sediment porewater evolution of the east central Atlantic Paleogene ocean margin revealed by U-Pb dating of sedimentary phosphates. Frontiers in Earth Science 10:997008. https://doi.org/10.3389/feart.2022.997008

Aubineau, J., Parat, F., Elghali, A., Raji, O., Addou, A., Bonnet, C., Muñoz, M., Mauguin, O., Baron, F., Jouti, M.B., Yazami, O.K., Bodinier, J.-L., 2022b. Highly variable content of fluorapatite-hosted CO_3^{2-} in the Upper Cretaceous/Paleogene phosphorites (Morocco) and implications for paleodepositional conditions. Chemical Geology 597, 120818. https://doi.org/10.1016/j.chemgeo.2022.120818

Aubineau, J., Parat, F., Pierson-Wickmann, A.-C., Séranne, M., Fru, E.C., El Bamiki, R., Elghali, A., Raji, O., Muñoz, M., Bonnet, C., Jourani, E.-S., Yazami, O.K., Bodinier, J.-L., 2024. Phosphate δ13Corg chemostratigraphy from the Gantour basin, Morocco: A proof of concept from the K–Pg transition to mid-Thanetian. Chemical Geology 121861. https://doi.org/10.1016/j.chemgeo.2023.121861

Babault, J., Van Den Driessche, J., Teixell, A., 2012. Longitudinal to transverse drainage network evolution in the High Atlas (Morocco): The role of tectonics. Tectonics 31. https://doi.org/10.1029/2011TC003015

Balestrieri, M.L., Moratti, G., Bigazzi, G., Algouti, A., 2009. Neogene exhumation of the Marrakech High Atlas (Morocco) recorded by apatite fission-track analysis. Terra Nova 21, 75–82. https://doi.org/10.1111/j.1365-3121.2008.00857.x

Balter, V., Blichert-Toft, J., Braga, J., Telouk, P., Thackeray, F., Albarède, F., 2008. U–Pb dating of fossil enamel from the Swartkrans Pleistocene hominid site, South Africa. Earth and Planetary Science Letters 267, 236–246. https://doi.org/10.1016/j.epsl.2007.11.039

Bau, M., Dulski, P., 1996. Distribution of yttrium and rare-earth elements in the Penge and Kuruman iron-formations, Transvaal Supergroup, South Africa. Precambrian Research 79, 37–55. https://doi.org/10.1016/0301-9268(95)00087-9

Bau, M., Möller, P., Dulski, P., 1997. Yttrium and lanthanides in eastern Mediterranean seawater and their fractionation during redox-cycling. Marine Chemistry 56, 123–131. https://doi.org/10.1016/S0304-4203(96)00091-6

Bonnet, C., Muñoz, M., Mathon, O., Motto-Ros, V., Elghali, A., Parat, F., Aubineau, J., Bodinier, J.-L., 2023. Sorption model for yttrium in fluorapatite: Geochemical implications. Geochemical Perspectives Letters 27, 2326. https://doi.org/10.7185/geochemlet.2326

Boujo, A., 1976. Contribution à l'étude géologique du gisement de phosphate crétacé-éocène des Ganntour (Maroc occidental). Sciences Géologiques, bulletins et mémoires 43.

Brigaud, B., Andrieu, S., Blaise, T., Haurine, F., Barbarand, J., 2021. Calcite uranium–lead geochronology applied to hardground lithification and sequence boundary dating. Sedimentology 68, 168–195. https://doi.org/10.1111/sed.12795

Brindley, G.W., Brown, G., 1980. Crystal structure of clay minerals and their X-ray identification. Mineralogical Society, London.

Burnett, W.C., Baker, K.B., Chin, P.A., McCabe, W., Ditchburn, R., 1988. Uranium-series and AMS ^{14}C studies of modern phosphatic pellets from Peru shelf muds. Marine Geology 80, 215–230.

Charton, R., Bertotti, G., Arnould, A.D., Storms, J.E.A., Redfern, J., 2021. Low-temperature thermochronology as a control on vertical movements for semi-quantitative source-to-sink analysis: A case study for the Permian to Neogene of Morocco and surroundings. Basin Research 33, 1337–1383. https://doi.org/10.1111/bre.12517

Chew, D.M., Petrus, J.A., Kamber, B.S., 2014. U–Pb LA–ICPMS dating using accessory mineral standards with variable common Pb. Chemical Geology 363, 185–199. https://doi.org/10.1016/j.chemgeo.2013.11.006

Compton, J.S., Bergh, E.W., 2016. Phosphorite deposits on the Namibian shelf. Marine Geology 380, 290–314. https://doi.org/10.1016/j.margeo.2016.04.006

Cosmidis, J., Benzerara, K., Gheerbrant, E., Estève, I., Bouya, B., Amaghzaz, M., 2013. Nanometer-scale characterization of exceptionally preserved bacterial fossils in Paleocene phosphorites from Ouled Abdoun (Morocco). Geobiology 11, 139–153. https://doi.org/10.1111/gbi.12022

De Baar, H.J.W., Brewer, P.G., Bacon, M.P., 1985. Anomalies in rare earth distributions in seawater:

Gd and Tb. Geochimica et Cosmochimica Acta 49, 1961–1969. https://doi.org/10.1016/0016-7037(85)90090-0

Döebelin, N., Kleeberg, R., 2015. Profex: a graphical user interface for the Rietveld refinement program BGMN. J Appl Cryst 48, 1573–1580. https://doi.org/10.1107/S1600576715014685

Domènech, M., Teixell, A., Stockli, D.F., 2016. Magnitude of rift-related burial and orogenic contraction in the Marrakech High Atlas revealed by zircon (U-Th)/He thermochronology and thermal modeling. Tectonics 35, 2609–2635. https://doi.org/10.1002/2016TC004283

Duggen, S., Hoernle, K.A., Hauff, F., Klügel, A., Bouabdellah, M., Thirlwall, M.F., 2009. Flow of Canary mantle plume material through a subcontinental lithospheric corridor beneath Africa to the Mediterranean. Geology 37, 283–286. https://doi.org/10.1130/G25426A.1

El Bamiki, R., Raji, O., Ouabid, M., Elghali, A., Khadiri Yazami, O., Bodinier, J.-L., 2021. Phosphate Rocks: A Review of Sedimentary and Igneous Occurrences in Morocco. Minerals 11, 1137. https://doi.org/10.3390/min11101137

El Bamiki, R., Séranne, M., Chellaï, E.H., Merzeraud, G., Marzoqi, M., Melinte-Dobrinescu, M.C., 2020. The Moroccan High Atlas phosphate-rich sediments: Unraveling the accumulation and differentiation processes. Sedimentary Geology 403, 105655. https://doi.org/10.1016/j.sedgeo.2020.105655

El Bamiki, R., Séranne, M., Parat, F., Aubineau, J., Chellaï, E.H., Marzoqi, M., Bodinier, J.-L., 2023. Post-phosphogenesis processes and the natural beneficiation of phosphates: Geochemical evidence from the Moroccan High Atlas phosphate-rich sediments. Chemical Geology 631, 121523. https://doi.org/10.1016/j.chemgeo.2023.121523

Ellouz, N., Patriat, M., Gaulier, J.-M., Bouatmani, R., Sabounji, S., 2003. From rifting to Alpine inversion: Mesozoic and Cenozoic subsidence history of some Moroccan basins. Sedimentary Geology 156, 185–212. https://doi.org/10.1016/S0037-0738(02)00288-9

Fassett, J.E., Heaman, L.M., Simonetti, A., 2011. Direct U-Pb dating of Cretaceous and Paleocene dinosaur bones, San Juan Basin, New Mexico. Geology 39, 159–162. https://doi.org/10.1130/G31466.1

Frizon de Lamotte, D., Zizi, M., Missenard, Y., Hafid, M., El Azzouzi, M., Maury, R.C., Charrière, A., Taki, Z., Benammi, M., Michard, A., 2008. The Atlas System, in: Michard, André, Saddiqi, O., Chalouan, A., Frizon de Lamotte, Dominique (Eds.), Continental Evolution: The Geology of Morocco: Structure, Stratigraphy, and Tectonics of the Africa-Atlantic-Mediterranean Triple Junction, Lecture Notes in Earth Sciences. Springer, Berlin, Heidelberg, pp. 133–202. https://doi.org/10.1007/978-3-540-77076-3_4

Frizon de Lamotte, D.F., Leturmy, P., Missenard, Y., Khomsi, S., Ruiz, G., Saddiqi, O., Guillocheau, F., Michard, A., 2009. Mesozoic and Cenozoic vertical movements in the Atlas system (Algeria, Morocco, Tunisia): An overview. Tectonophysics 475, 9–28. https://doi.org/10.1016/j.tecto.2008.10.024

Garnit, H., Bouhlel, S., Barca, D., Chtara, C., 2012. Application of LA-ICP-MS to sedimentary phosphatic particles from Tunisian phosphorite deposits: Insights from trace elements and REE into paleo-depositional environments. Geochemistry 72, 127–139. https://doi.org/10.1016/j.chemer.2012.02.001

Gasquet, D., Levresse, G., Cheilletz, A., Azizi-Samir, M.R., Mouttaqi, A., 2005. Contribution to a geodynamic reconstruction of the Anti-Atlas (Morocco) during Pan-African times with the emphasis on inversion tectonics and metallogenic activity at the Precambrian–Cambrian transition. Precambrian Research 140, 157–182. https://doi.org/10.1016/j.precamres.2005.06.009

Glenn, C.R., Arthur, M.A., Yeh, H., Burnett, W.C., 1988. Carbon isotopic composition and lattice-bound carbonate of Peru-Chile margin phosphorites. Marine Geology 80, 287–307.

Greene, S., Heaman, L.M., DuFrane, S.A., Williamson, T., Currie, P.J., 2018. Introducing a geochemical screen to identify geologically meaningful U-Pb dates in fossil teeth. Chemical Geology 493, 1–15.

Griffin, W.L., 2008. GLITTER: Data reduction software for laser ablation ICP-MS. Laser Ablation ICP-MS in the Earth Sciences : Current practices and outstanding issues 308–311.

Hafid, M., Zizi, M., Bally, A.W., Ait Salem, A., 2006. Structural styles of the western onshore and offshore termination of the High Atlas, Morocco. Comptes Rendus Geoscience, Quelques développements récents sur la géodynamique du Maghreb 338, 50–64. https://doi.org/10.1016/j.crte.2005.10.007

Haley, B.A., Klinkhammer, G.P., McManus, J., 2004. Rare earth elements in pore waters of marine sediments. Geochimica et Cosmochimica Acta 68, 1265–1279. https://doi.org/10.1016/j.gca.2003.09.012

Herwartz, D., Münker, C., Tütken, T., Hoffmann, J.E., Wittke, A., Barbier, B., 2013. Lu–Hf isotope

systematics of fossil biogenic apatite and their effects on geochronology. Geochimica et Cosmochimica Acta 101, 328–343.
Herwartz, D., Tütken, T., Münker, C., Jochum, K.P., Stoll, B., Sander, P.M., 2011. Timescales and mechanisms of REE and Hf uptake in fossil bones. Geochimica et Cosmochimica Acta 75, 82–105.
Jaffal, M., Charbaoui, A., Kchikach, A., El Ghorfi, M., Khaldoun, A., El Mahdi Safhi, A., Bodinier, J.-L., Yazami, O.K., Jourani, E.-S., Manar, A., 2022. Gravity study of the Western Bahira Basin and the Gantour Phosphatic Plateau, central Morocco: Interpretation and hydrogeological implications. Journal of African Earth Sciences 193, 104581. https://doi.org/10.1016/j.jafrearsci.2022.104581
Kocsis, L., Gheerbrant, E., Mouflih, M., Cappetta, H., Ulianov, A., Chiaradia, M., Bardet, N., 2016. Gradual changes in upwelled seawater conditions (redox, pH) from the late Cretaceous through early Paleogene at the northwest coast of Africa: Negative Ce anomaly trend recorded in fossil bio-apatite. Chemical Geology 421, 44–54. https://doi.org/10.1016/j.chemgeo.2015.12.001
Kocsis, L., Gheerbrant, E., Mouflih, M., Cappetta, H., Yans, J., Amaghzaz, M., 2014. Comprehensive stable isotope investigation of marine biogenic apatite from the late Cretaceous–early Eocene phosphate series of Morocco. Palaeogeography, Palaeoclimatology, Palaeoecology 394, 74–88. https://doi.org/10.1016/j.palaeo.2013.11.002
Kocsis, L., Trueman, C.N., Palmer, M.R., 2010. Protracted diagenetic alteration of REE contents in fossil bioapatites: Direct evidence from Lu–Hf isotope systematics. Geochimica et Cosmochimica Acta 74, 6077–6092. https://doi.org/10.1016/j.gca.2010.08.007
Kocsis, L., Ulianov, A., Mouflih, M., Khaldoune, F., Gheerbrant, E., 2021. Geochemical investigation of the taphonomy, stratigraphy, and palaeoecology of the mammals from the Ouled Abdoun Basin (Paleocene-Eocene of Morocco). Palaeogeography, Palaeoclimatology, Palaeoecology 577, 110523. https://doi.org/10.1016/j.palaeo.2021.110523
Koeppenkastrop, D., De Carlo, E.H., 1992. Sorption of rare-earth elements from seawater onto synthetic mineral particles: An experimental approach. Chemical Geology 95, 251–263. https://doi.org/10.1016/0009-2541(92)90015-W
Lanari, R., Fellin, M.G., Faccenna, C., Balestrieri, M.L., Pazzaglia, F.J., Youbi, N., Maden, C., 2020. Exhumation and Surface Evolution of the Western High Atlas and Surrounding Regions as Constrained by Low-Temperature Thermochronology. Tectonics 39, e2019TC005562. https://doi.org/10.1029/2019TC005562
LeGeros, P.G., Trautz, O.R., LeGeros, J.P., Klein, E., Shirra, W.P., 1967. Apatite crystallites: Effects of carbonate on morphology. Science 155, 1409–1411.
Leprêtre, R., Missenard, Y., Barbarand, J., Gautheron, C., Jouvie, I., Saddiqi, O., 2018. Polyphased Inversions of an Intracontinental Rift: Case Study of the Marrakech High Atlas, Morocco. Tectonics 37, 818–841. https://doi.org/10.1002/2017TC004693
Li, D., Peng, J., Chew, D., Liang, Y., Hollings, P., Fu, Y., Dong, Y., Sun, X., 2023. Dating rare earth element enrichment in deep-sea sediments using U-Pb geochronology of bioapatite. Geology. https://doi.org/10.1130/G50938.1
Lotfi, F., Belkabir, A., Brown, A.C., Marcoux, E., Brunet, S., Maacha, L., 2008. Geology and Mineralogy of the Hercynian Koudiat Aïcha Polymetallic (Zn-Pb-Cu) Massive Sulfide Deposit, Central Jebilet, Morocco. Exploration and Mining Geology 17, 145–162. https://doi.org/10.2113/gsemg.17.3-4.145
Lumiste, K., Mänd, K., Bailey, J., Paiste, P., Lang, L., Lepland, A., Kirsimäe, K., 2019. REE+Y uptake and diagenesis in Recent sedimentary apatites. Chemical Geology 525, 268–281. https://doi.org/10.1016/j.chemgeo.2019.07.034
Luo, Y., Hughes, J.M., Rakovan, J., Pan, Y., 2009. Site preference of U and Th in Cl, F, and Sr apatites. American Mineralogist 94, 345–351. https://doi.org/10.2138/am.2009.3026
Mänd, K., Kirsimäe, K., Lepland, A., Crosby, C.H., Bailey, J.V., Konhauser, K.O., Wirth, R., Schreiber, A., Lumiste, K., 2018. Authigenesis of biomorphic apatite particles from Benguela upwelling zone sediments off Namibia: The role of organic matter in sedimentary apatite nucleation and growth. Geobiology 16, 640–658. https://doi.org/10.1111/gbi.12309
McClellan, G.H., Van Kauwenbergh, S.J., 1991. Mineralogical and chemical variation of francolites with geological time. Journal of the Geological Society 148, 809–812. https://doi.org/10.1144/gsjgs.148.5.0809
McDowell, F.W., McIntosh, W.C., Farley, K.A., 2005. A precise ^{40}Ar–^{39}Ar reference age for the Durango apatite (U–Th)/He and fission-track dating standard. Chemical Geology 214, 249–263. https://doi.org/10.1016/j.chemgeo.2004.10.002
Michard, A., Saddiqi, O., Chalouan, A., Frizon de Lamotte, D., 2008. Continental Evolution: The Geology of Morocco. Springer, Berlin, Heidelberg.
Missenard, Y., Saddiqi, O., Barbarand, J., Leturmy, P., Ruiz, G., El Haimer, F.-Z., Frizon de Lamotte,

D., 2008. Cenozoic denudation in the Marrakech High Atlas, Morocco: insight from apatite fission-track thermochronology. Terra Nova 20, 221–228. https://doi.org/10.1111/j.1365-3121.2008.00810.x

Missenard, Y., Zeyen, H., Frizon de Lamotte, D., Leturmy, P., Petit, C., Sébrier, M., Saddiqi, O., 2006. Crustal versus asthenospheric origin of relief of the Atlas Mountains of Morocco. Journal of Geophysical Research: Solid Earth 111, B03401. https://doi.org/10.1029/2005JB003708

Molnár, Z., Kiss, G.B., Dunkl, I., Czuppon, G., Zaccarini, F., Dódony, I., 2018. Geochemical characteristics of Triassic and Cretaceous phosphorite horizons from the Transdanubian Mountain Range (western Hungary): genetic implications. Mineral. mag. 82, S147–S171. https://doi.org/10.1180/minmag.2017.081.103

Nathan, Y., 1984. The Mineralogy and Geochemistry of Phosphorites, in: Nriagu, J.O., Moore, P.B. (Eds.), Phosphate Minerals. Springer-Verlag, Berlin, Heidelberg, pp. 275–291.

Nguidi, M.A., Mouflih, M., Benbouziane, A., Kocsis, L., El Ouariti, S., El Boukhari, H., Aquit, M., Yazami, O.K., 2021. Lithofacies analysis, sedimentary dynamics and genesis of Maastrichtian-Eocene phosphorites of BouCraa deposit (Southern Morocco). Journal of African Earth Sciences 177, 104161. https://doi.org/10.1016/j.jafrearsci.2021.104161

OCP, 1989. The phosphate basins of Morocco, in: Notholt, A.J.G., Sheldon, R.P., Davidson, D.F. (Eds.), Phosphate Deposits of the World, Vol. 2: Phosphate Rock Resources. Cambridge, United Kingdom, pp. 301–311.

O'Sullivan, G.J., Daly, J.S., Murray, J., Ó'Gogáin, A., Chew, D.M., Drakou, F., Guyett, P.C., Badenszki, E., Hoare, B.C., 2021. Uranium–lead phosphate chronostratigraphy: A proof of concept from the mid-Carboniferous boundary. Sedimentary Geology 422, 105961. https://doi.org/10.1016/j.sedgeo.2021.105961

Pan, Y., Fleet, M.E., 2002. Compositions of the Apatite-Group Minerals: Substitution Mechanisms and Controlling Factors. Reviews in Mineralogy and Geochemistry 48, 13–49. https://doi.org/10.2138/rmg.2002.48.2

Pearce, N.J., Perkins, W.T., Westgate, J.A., Gorton, M.P., Jackson, S.E., Neal, C.R., Chenery, S.P., 1997. A compilation of new and published major and trace element data for NIST SRM 610 and NIST SRM 612 glass reference materials. Geostandards newsletter 21, 115–144.

Planavsky, N.J., Bekker, A., Rouxel, O.J., Kamber, B., Hofmann, A., Knudsen, A., Lyons, T.W., 2010. Rare earth element and yttrium compositions of Archean and Paleoproterozoic Fe formations revisited: New perspectives on the significance and mechanisms of deposition. Geochimica et Cosmochimica Acta 74, 6387–6405. https://doi.org/10.1016/j.gca.2010.07.021

Pufahl, P.K., Grimm, K.A., 2003. Coated phosphate grains: Proxy for physical, chemical, and ecological changes in seawater. Geol 31, 801–804. https://doi.org/10.1130/G19658.1

Pufahl, P.K., Groat, L.A., 2017. Sedimentary and Igneous Phosphate Deposits: Formation and Exploration: An Invited Paper. Economic Geology 112, 483–516. https://doi.org/10.2113/econgeo.112.3.483

Reynard, B., Lécuyer, C., Grandjean, P., 1999. Crystal-chemical controls on rare-earth element concentrations in fossil biogenic apatites and implications for paleoenvironmental reconstructions. Chemical Geology 155, 233–241. https://doi.org/10.1016/S0009-2541(98)00169-7

Roberts, N.M.W., Drost, K., Horstwood, M.S.A., Condon, D.J., Chew, D., Drake, H., Milodowski, A.E., McLean, N.M., Smye, A.J., Walker, R.J., Haslam, R., Hodson, K., Imber, J., Beaudoin, N., Lee, J.K., 2020. Laser ablation inductively coupled plasma mass spectrometry (LA-ICP-MS) U–Pb carbonate geochronology: strategies, progress, and limitations. Geochronology 2, 33–61. https://doi.org/10.5194/gchron-2-33-2020

Rochín-Bañaga, H., Davis, D.W., 2023. Insights into U-Th-Pb mobility during diagenesis from laser ablation U-Pb dating of apatite fossils. Chemical Geology 618, 121290. https://doi.org/10.1016/j.chemgeo.2022.121290

Rochín-Bañaga, H., Davis, D.W., Moysiuk, J., 2024. U–Pb dating of belemnites and rugose corals: The potential for absolute dating of calcitic invertebrate fossils. Chemical Geology 121862. https://doi.org/10.1016/j.chemgeo.2023.121862

Rochín-Bañaga, H., Davis, D.W., Schwennicke, T., 2021. First U-Pb dating of fossilized soft tissue using a new approach to paleontological chronometry. Geology 49, 1027–1031. https://doi.org/10.1130/G48386.1

Rossi, M., Tarrieu, L., Cheilletz, A., Gasquet, D., Deloule, E., Paquette, J.-L., Bounajma, H., Mantoy, T., Ouazzani, L., Ouchtouban, L., 2016. The Polymetallic (W–Au and Pb–Zn–Ag) Tighza District (Central Morocco): Ages of Magmatic and Hydrothermal Events, in: Bouabdellah, M., Slack, J.F. (Eds.), Mineral Deposits of North Africa. Springer International Publishing, Cham, pp. 107–131. https://doi.org/10.1007/978-3-319-31733-5_3

Saddiqi, O., El Haimer, F.-Z., Michard, A., Barbarand, J., Ruiz, G.M.H., Mansour, E.M., Leturmy, P.,

Frizon de Lamotte, D., 2009. Apatite fission-track analyses on basement granites from south-western Meseta, Morocco: Paleogeographic implications and interpretation of AFT age discrepancies. Tectonophysics, The geology of vertical movements of the lithosphere 475, 29–37. https://doi.org/10.1016/j.tecto.2009.01.007

Salvan, H., 1955. Les invertébrés fossiles des phosphates marocains. Notes et Memoires du Service Geologique du Maroc 93, 1–258.

Sano, Y., Terada, K., Ly, C.V., Park, E.J., 2006. Ion microprobe U-Pb dating of a dinosaur tooth. Geochemical Journal 40, 171–179.

Schuffert, J.D., Kastner, M., Emanuele, G., Jahnke, R.A., 1990. Carbonate-ion substitution in francolite: A new equation. Geochimica et Cosmochimica Acta 54, 2323–2328. https://doi.org/10.1016/0016-7037(90)90058-S

Shields, G., Stille, P., 2001. Diagenetic constraints on the use of cerium anomalies as palaeoseawater redox proxies: an isotopic and REE study of Cambrian phosphorites. Chemical Geology, Response of the Oceanic / Atmospheric Systems to Past Global Changes 175, 29–48. https://doi.org/10.1016/S0009-2541(00)00362-4

Singer, A., Galan, E., 1984. Palygorskite-Sepiolite: Occurrences, Genesis and Uses. Elsevier, Amsterdam.

Spencer, C.J., Kirkland, C.L., Taylor, R.J.M., 2016. Strategies towards statistically robust interpretations of *in situ* U–Pb zircon geochronology. Geoscience Frontiers 7, 581–589. https://doi.org/10.1016/j.gsf.2015.11.006

Stacey, J.S., Kramers, J.D., 1975. Approximation of terrestrial lead isotope evolution by a two-stage model. Earth and Planetary Science Letters 26, 207–221. https://doi.org/10.1016/0012-821X(75)90088-6

Taylor, S.R., McLennan, S.M., 1985. The continental crust: Its composition and evolution. Blackwell Scientific Puplications, Oxford.

Teixell, A., Arboleya, M.-L., Julivert, M., Charroud, M., 2003. Tectonic shortening and topography in the central High Atlas (Morocco). Tectonics 22. https://doi.org/10.1029/2002TC001460

Teixell, A., Ayarza, P., Zeyen, H., Fernandez, M., Arboleya, M.-L., 2005. Effects of mantle upwelling in a compressional setting: the Atlas Mountains of Morocco. Terra Nova 17, 456–461.

Trappe, J. (Ed.), 1998. The processes: Phosphogenesis and phosphorite genesis, in: Phanerozoic Phosphorite Depositional Systems: A Dynamic Model for a Sedimentary Resource System, Lecture Notes in Earth Sciences. Springer, Berlin, Heidelberg, pp. 59–214. https://doi.org/10.1007/BFb0009673

Vermeesch, P., 2018. IsoplotR: A free and open toolbox for geochronology. Geoscience Frontiers, SPECIAL ISSUE: Frontiers in geoscience:A tribute to Prof. Xuanxue Mo 9, 1479–1493. https://doi.org/10.1016/j.gsf.2018.04.001

Wendt, I., Carl, C., 1991. The statistical distribution of the mean squared weighted deviation. Chemical Geology: Isotope Geoscience section 86, 275–285. https://doi.org/10.1016/0168-9622(91)90010-T

Yang, H., Zhao, Z., Xia, Y., Xiao, J., 2021. REY enrichment mechanisms in the early Cambrian phosphorite from South China. Sedimentary Geology 426, 106041. https://doi.org/10.1016/j.sedgeo.2021.106041

Yans, J., Amaghzaz, M., Bouya, B., Cappetta, H., Iacumin, P., Kocsis, L., Mouflih, M., Selloum, O., Sen, S., Storme, J.-Y., Gheerbrant, E., 2014. First carbon isotope chemostratigraphy of the Ouled Abdoun phosphate Basin, Morocco; implications for dating and evolution of earliest African placental mammals. Gondwana Research 25, 257–269. https://doi.org/10.1016/j.gr.2013.04.004

Zouhri, S., Kchikach, A., Saddiqi, O., Haïmer, F.Z.E., Baidder, L., Michard, A., 2008. The Cretaceous-Tertiary Plateaus, in: Michard, André, Saddiqi, Omar, Chalouan, A., Lamotte, D.F. de (Eds.), Continental Evolution: The Geology of Morocco: Structure, Stratigraphy, and Tectonics of the Africa-Atlantic-Mediterranean Triple Junction, Lecture Notes in Earth Sciences. Springer, Berlin, Heidelberg, pp. 331–358. https://doi.org/10.1007/978-3-540-77076-3_7

Figure and table legends

Figure 1: (a) Simplified map of northwestern Morocco showing the main Atlas fault systems and Upper Cretaceous-Paleogene phosphate basins (orange). NJF, north Jebilet front; WM, western Meseta; WHA, western High Atlas; CHA, central High Atlas; MA, Middle Atlas. (b) Simplified structural map of the western High Atlas in Morocco, modified from El Bamiki et al. (2020). Red arrows indicate the location of studied sites and sections. ER, Erguita; AMZ, Amizmiz; MB, Moulay Brahim; TAL, Talentloute; NAF, north Atlas front.

Figure 2: Synthetic lithostratigraphic columns of the western Gantour Plateau, modified from Aubineau et al. (2024) (a) and WHA sections, modified from El Bamiki et al. (2020) (b). C2M level corresponds to the uppermost Maastrichtian. All phosphate-bearing rocks in the WHA were sampled from the maximum flooding interval or immediately above. The red and blue shadings are the transgressive surface and the maximum flooding zone set as a reference datum for horizontalization, respectively. Key nannofossil Zones are in black. Radiometric U-Pb ages are from Aubineau et al. (2022a). Note differences in thickness between the studied sections.

Figure 3: Petrographic characteristics of the studied samples. Selected areas for *in situ* analyses, among others. (a) Initial visual of CFA peloids by binocular microscopy. Scale bar is 1 mm. SEM images in backscattered electron mode of Gantour (b, c), Moulay Brahim (d-f), Talentloute (g-i), and Erguita (j-l) phosphate-bearing samples. Note the dashed lines showing the irregular phosphatic layers after transport in the Gantour phosphorites. Ca, calcite; Do, dolomite; Q, quartz; CFA, carbonate fluorapatite; CM, clayey matrix; Mi, Microcline. EDX analyses were performed to allow mineral identification. Scale bars of SEM images are 500 µm.

Figure 4: REEY geochemistry of the WHA (Amizmiz, Moulay Brahim, and Talentloute) and Gantour phosphorites. (a) Box plot of REE content of CFA. The box shows 50% of the data, and whiskers extend to 1.5 times the interquartile range. The bar of the box plot, red square, and black diamonds are the median, mean, and outliers, respectively. (b) Average PAAS-normalized REEY patterns compared to modern seawater (Alibo and Nozaki, 1999). Light (L)REE (La to Nd), Middle (M)REE

(Sm to Dy), and Heavy (H)REE (Ho to Lu). Geochemical data of Amizmiz samples and PAAS are from Aubineau et al. (2022a) and Taylor and McLennan (1985), respectively.

Figure 5: $REEY_{SN}$ binary diagrams of the WHA (Amizmiz, Moulay Brahim, and Talentloute) and Gantour phosphorites. Average $REEY_{SN}$ values are represented only and reported at 1 standard deviation. The number of analyses from each phosphorite horizon is shown in Figure 3. (a) $(Sm/Yb)_{SN}$ vs. $(Sm/Pr)_{SN}$, after (Garnit et al., 2012). (b) Ce anomaly vs. Pr anomaly, after (Bau and Dulski, 1996). Field (I), no La and Ce anomalies; Fields IIa and IIb, apparent negative and positive Ce resulted from positive and negative La anomaly, respectively; Fields IIIa and IIIb, true positive and negative Ce anomaly, respectively. (c) $(La/Yb)_{SN}$ vs. $(La/Sm)_{SN}$, after (Reynard et al., 1999). (d) Y anomaly vs. $(La/Nd)_{SN}$, after (Shields and Stille, 2001). While red squares correspond to the mean $REEY_{SN}$ value (n = 22, 1 standard deviation) of unaltered CFA in recent Namibian phosphorites (Lumiste et al., 2019), geochemical data of Amizmiz samples and PAAS are from (Aubineau et al., 2022a) and Taylor and McLennan (1985), respectively.

Figure 6: Tera-Wasserburg concordia diagrams from the Gantour Plateau (a), Southern front of the WHA (Erguita samples) (b), and Northern front of the WHA (Amizmiz, Moulay Brahim, and Talentloute samples from top to bottom, respectively) (c). The U-Pb dates of the AMZ phosphorites are modified from Aubineau et al. (2022a), with the green and purple lines representing unanchored discordias of the AMZ8-AMZ9 and AMZ13 samples, respectively. Age calculations do not include unfilled ellipses as the corresponding data are considerably outside of error along the mixing line probably caused by the heterogeneous nature of CFA peloids. Errors and ellipses are reported at 2 standard errors. MSWD, Mean Squared Weighted deviation. n, number of analyses corresponding to the number of laser spots.

Figure 7: Comparison of the known stratigraphic age of studied rocks with the LA-ICP-MS U-Pb dates. Three U-Pb dates define one stratigraphic interval (orange dotted ellipse). One U-Pb date also characterizes three distinct stratigraphic levels (black dotted ellipse). Error bars are in red. ER, Erguita; AMZ, Amizmiz; MB, Moulay Brahim; TAL, Talentloute.

Figure 8: Conceptual model showing the temporal evolution of the Gantour and WHA samples during subsiding and uplift phases. (a) Northern front of the WHA. (1) Phosphorite formation during the maximum flooding interval or immediately after. (2) Burial associated with a ~20 m/Ma sedimentation rate has led CFA crystallites to behave as a closed system at ~43 and ~35.3 Ma. (3) Exhumation of the outer WHA units. (4) Present-day elevation (>1000 m) of the samples. Phosphorites are preserved at the surface and hosted in large-scale synclines. (b) Southern front of the WHA. (1) Formation of turbiditic phosphate-bearing sediments during the maximum flooding interval or immediately after. (2) Open system behavior of CFA at the Eocene-Oligocene transition, despite a burial associated with a ≥20 m/Ma sedimentation rate. (3) Uplift of the Erguita section, resulting in system closure at the Oligocene-Miocene transition. (4) Present-day elevation (>400 m) of the samples that are preserved at the surface. A gentle southward dip characterizes the Erguita strata. (c) Gantour Plateau. (I) Phosphorite formation. (II) Burial associated with a ~2 m/Ma sedimentation rate did not facilitate the closed system behavior of CFA crystallites. (III) Uplift of the Gantour Plateau led to the closure of the U-Pb system at the Oligocene-Miocene transition. (4) Present-day elevation (~400 m) of the samples. Phosphorites are not present at the surface. White arrow size represents the proportion of initial radiogenic Pb in CFA. MFZ, maximum flooding zone. Vertical and horizontal scales are not represented. The length of each panel corresponds relatively to the thickness of the sedimentary column.

Table 1: XRD reflections and estimated CO_3^{2-} contents (wt.%) for the Gantour and WHA phosphate-bearing rocks. The carbonate concentration (wt.%) in CFA grains is calculated as $10.643x^2 - 52.512x + 56.986$ where x stands for $\Delta 2\theta(004–410)$ (Schuffert et al., 1990). DSP1 and C2M are phosphorite levels.

	Section	Sample	Height (m)	(410) Å	(004) Å	(410) °2θ	(004) °2θ	$\Delta 2\theta$	CO_3^{2-} content
Western Gantour basin		DSP1†	*27.53*	1.76195	1.72324	51.849	53.104	1.255	7.9
		C2M**	*35.43*	1.76262	1.72303	51.828	53.111	1.283	7.1
Northern front of the	Moulay Brahim	D-MB4§	100.0	1.76175	1.7239	51.855	53.082	1.226	8.6
		D-	94.3	1.761	1.723	51.862	53.079	1.21	8.8

WHA		MB3§		54	98			7	
		D-MB2§	93.4	1.76073	1.72373	51.888	53.087	1.200	9.3
	Talentloute	D-TAL3§	86.4	1.76214	1.72382	51.843	53.084	1.241	8.2
		D-TAL2§	85.6	1.7622	1.72415	51.841	53.073	1.232	8.4
		D-TAL1§	85.1	1.76189	1.72386	51.851	53.083	1.232	8.4
	Amizmiz	AMZ13#		1.76150	1.72321	51.863	53.105	1.241	8.2
		AMZ9#		1.76215	1.72363	51.843	53.091	1.248	8.0
		AMZ8#		1.76180	1.72368	51.854	53.089	1.235	8.4
Southern front of the WHA	Erguita	D-ER4	87.6	1.76685	1.72399	51.695	53.079	1.384	4.7
		D-ER3	87.0	1.76582	1.72336	51.727	53.100	1.373	5.0
		D-ER2	86.5	1.7648	1.72295	51.759	53.113	1.354	5.4
		D-ER1	85.4	1.76545	1.72302	51.739	53.111	1.372	5.0

†: published in Aubineau et al. (2022b)

**: published in Aubineau et al. (2024)

§: published in El Bamiki et al. (2023)

#: published in Aubineau et al. (2022a)

Declaration of interests

☒ The authors declare that they have no known competing financial interests or personal relationships that could have appeared to influence the work reported in this paper.

☐The authors declare the following financial interests/personal relationships which may be considered as potential competing interests:

- U-Pb dating of authigenic carbonate fluorapatite (CFA) peloids in northwestern Morocco
- Long-term open system behavior of CFA minerals
- U-Pb dates younger than the expected stratigraphic ages by 25 to 40 Ma
- Incorporation of unsupported radiogenic Pb during reequilibration
- Burial diagenesis and uplift as plausible caused for system closure of CFA

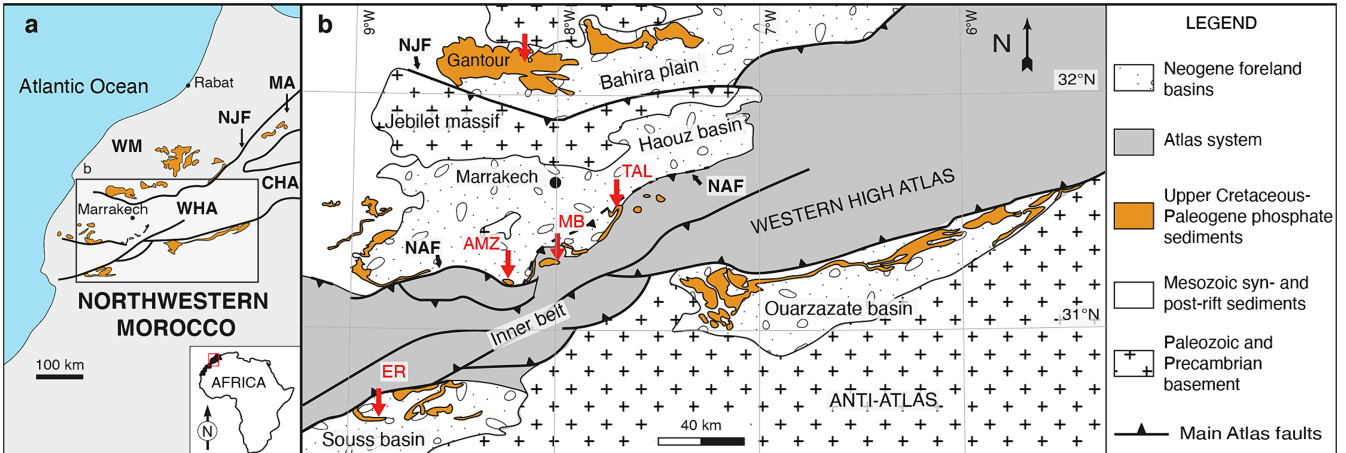
a
Atlantic Ocean
Rabat
MA
NJF
WM
b
CHA
Marrakech
WHA
NORTHWESTERN
MOROCCO
100 km
AFRICA
N
b
9°W
8°W
7°W
6°W
NJF
Gantour
Bahira plain
Jebilet massif
Haouz basin
Marrakech
TAL
NAF
WESTERN HIGH ATLAS
MB
AMZ
NAF
Ouarzazate basin
Inner belt
ER
ANTI-ATLAS
Souss basin
40 km
N
32°N
31°N
LEGEND
Neogene foreland basins
Atlas system
Upper Cretaceous-Paleogene phosphate sediments
Mesozoic syn- and post-rift sediments
Paleozoic and Precambrian basement
Main Atlas faults

Figure 1

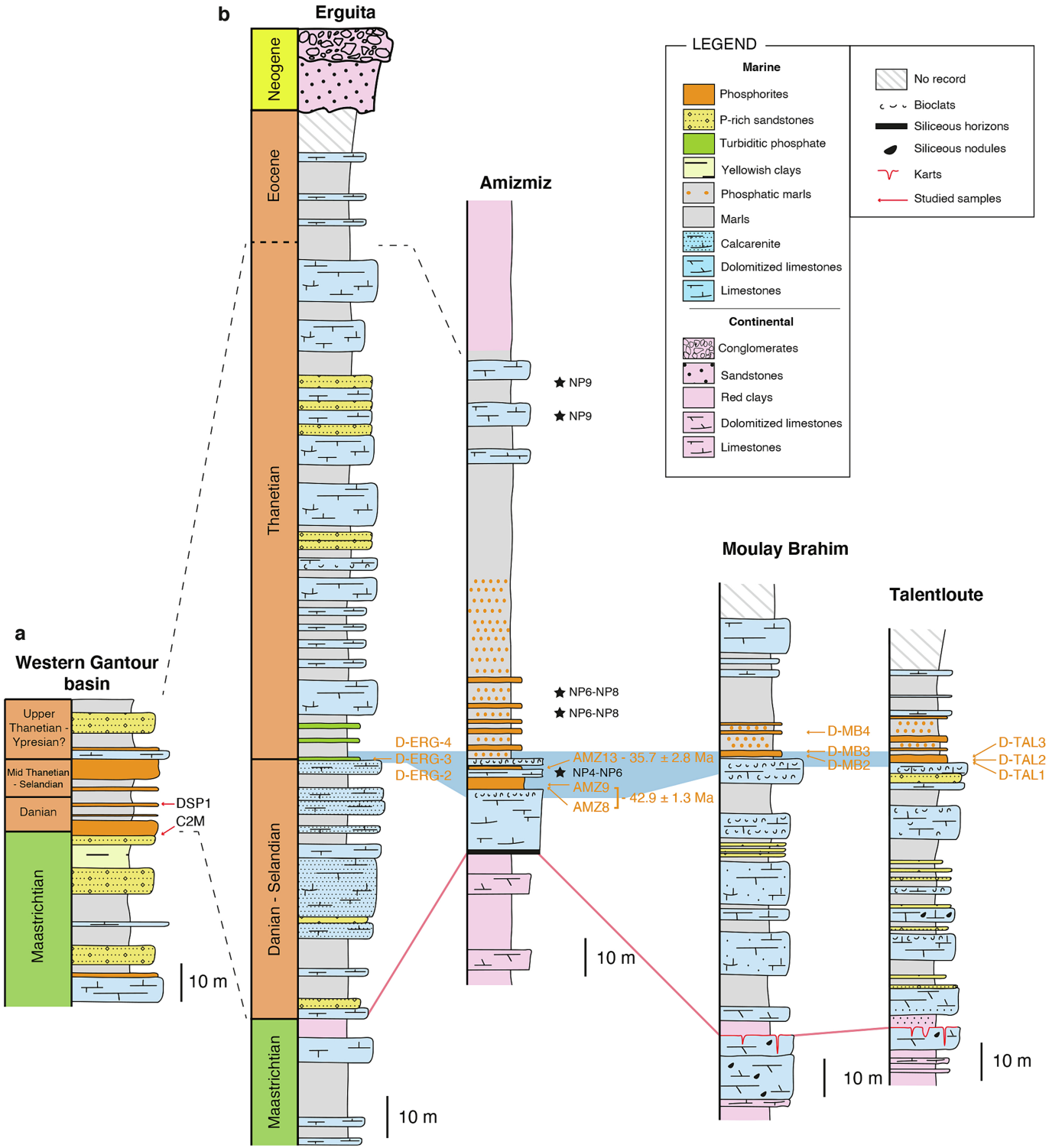
a
Western Gantour basin
Upper Thanetian - Ypresian?
Mid Thanetian - Selandian
Danian
Maastrichtian
DSP1
C2M
10 m
b
Erguita
Neogene
Eocene
Thanetian
Danian - Selandian
Maastrichtian
10 m
Amizmiz
NP9
NP9
NP6-NP8
NP6-NP8
D-ERG-4
D-ERG-3
D-ERG-2
AMZ13 - 35.7 ± 2.8 Ma
NP4-NP6
AMZ9
AMZ8
42.9 ± 1.3 Ma
10 m
Moulay Brahim
D-MB4
D-MB3
D-MB2
10 m
Talentloute
D-TAL3
D-TAL2
D-TAL1
10 m
LEGEND
Marine
Phosphorites
P-rich sandstones
Turbiditic phosphate
Yellowish clays
Phosphatic marls
Marls
Calcarenite
Dolomitized limestones
Limestones
Continental
Conglomerates
Sandstones
Red clays
Dolomitized limestones
Limestones
No record
Bioclats
Siliceous horizons
Siliceous nodules
Karts
Studied samples

Figure 2

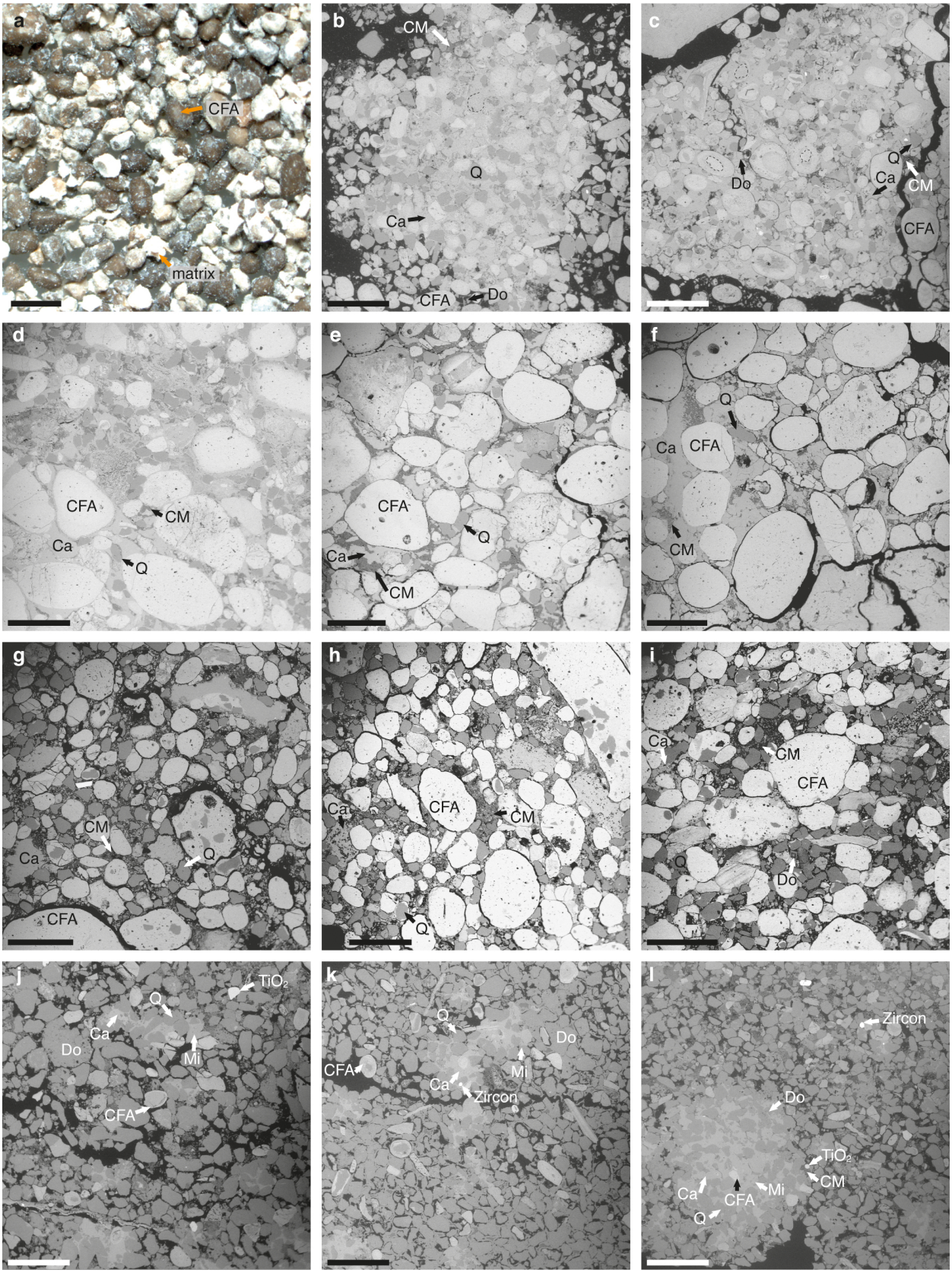
a
CFA
matrix
b
CM
Q
Ca
CFA
Do
c
Do
Q
Ca
CM
CFA
d
CFA
CM
Ca
Q
e
CFA
Q
Ca
CM
f
Q
Ca
CFA
CM
g
CM
Ca
Q
CFA
h
Ca
CFA
CM
Q
i
Ca
CM
CFA
Q
Do
j
TiO2
Q
Ca
Do
Mi
CFA
k
Q
Do
CFA
Mi
Ca
Zircon
l
Zircon
Do
TiO2
CM
Ca
CFA
Mi
Q

Figure 3

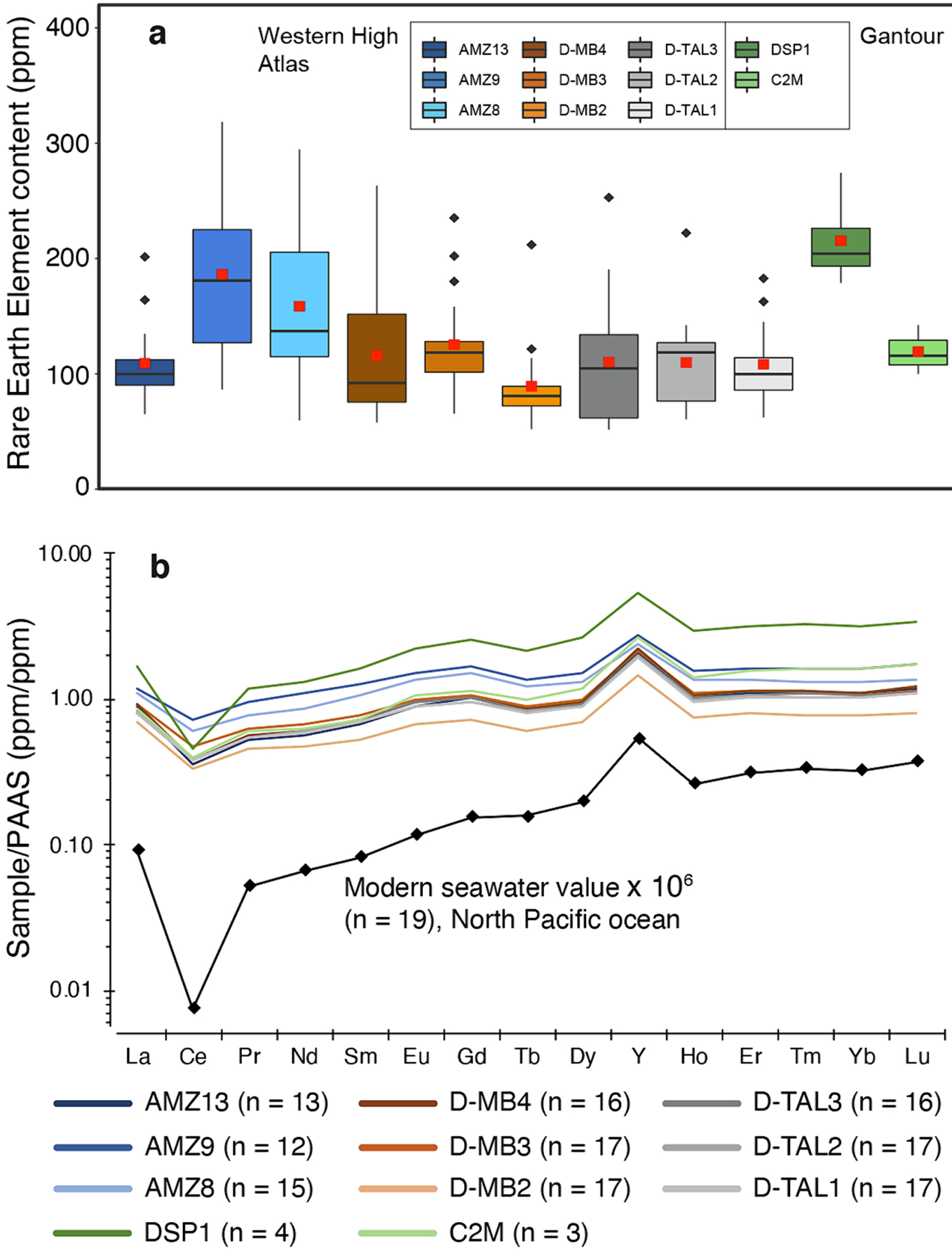
a
Western High Atlas
Gantour
AMZ13
AMZ9
AMZ8
D-MB4
D-MB3
D-MB2
D-TAL3
D-TAL2
D-TAL1
DSP1
C2M
Rare Earth Element content (ppm)
400
300
200
100
0
b
Sample/PAAS (ppm/ppm)
10.00
1.00
0.10
0.01
Modern seawater value x 10⁶
(n = 19), North Pacific ocean
La
Ce
Pr
Nd
Sm
Eu
Gd
Tb
Dy
Y
Ho
Er
Tm
Yb
Lu
AMZ13 (n = 13)
AMZ9 (n = 12)
AMZ8 (n = 15)
DSP1 (n = 4)
D-MB4 (n = 16)
D-MB3 (n = 17)
D-MB2 (n = 17)
C2M (n = 3)
D-TAL3 (n = 16)
D-TAL2 (n = 17)
D-TAL1 (n = 17)

Figure 4

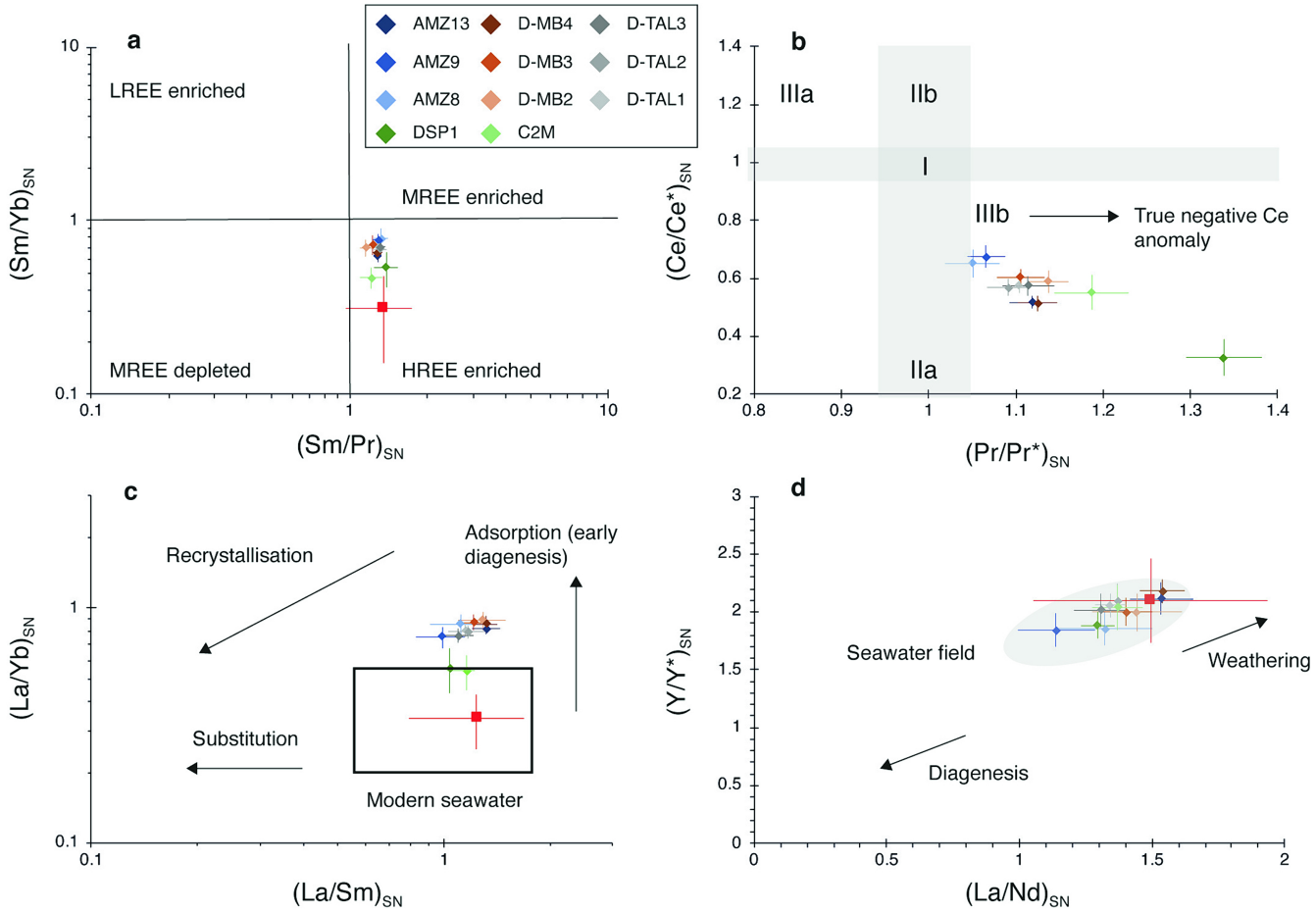
a
AMZ13
AMZ9
AMZ8
DSP1
D-MB4
D-MB3
D-MB2
C2M
D-TAL3
D-TAL2
D-TAL1
LREE enriched
MREE enriched
MREE depleted
HREE enriched
(Sm/Yb)SN
(Sm/Pr)SN
b
IIIa
IIb
I
IIIb
IIa
True negative Ce anomaly
(Ce/Ce*)SN
(Pr/Pr*)SN
c
Recrystallisation
Adsorption (early diagenesis)
Substitution
Modern seawater
(La/Yb)SN
(La/Sm)SN
d
Seawater field
Weathering
Diagenesis
(Y/Y*)SN
(La/Nd)SN

Figure 5

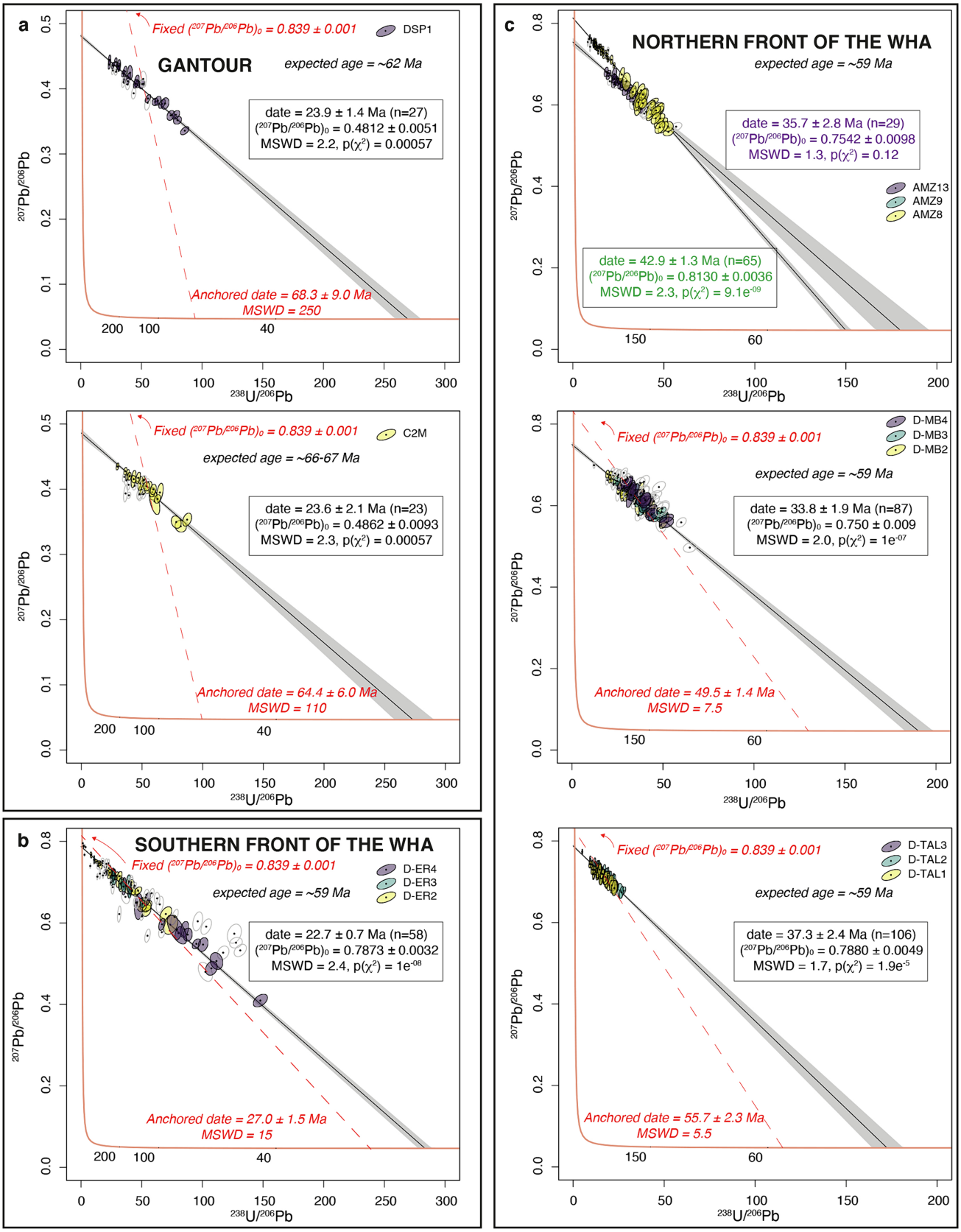
a
GANTOUR
expected age = ~62 Ma
Fixed (207Pb/206Pb)0 = 0.839 ± 0.001
DSP1
date = 23.9 ± 1.4 Ma (n=27)
(207Pb/206Pb)0 = 0.4812 ± 0.0051
MSWD = 2.2, p(χ2) = 0.00057
Anchored date = 68.3 ± 9.0 Ma
MSWD = 250
C2M
expected age = ~66-67 Ma
date = 23.6 ± 2.1 Ma (n=23)
(207Pb/206Pb)0 = 0.4862 ± 0.0093
MSWD = 2.3, p(χ2) = 0.00057
Anchored date = 64.4 ± 6.0 Ma
MSWD = 110
b
SOUTHERN FRONT OF THE WHA
expected age = ~59 Ma
D-ER4
D-ER3
D-ER2
date = 22.7 ± 0.7 Ma (n=58)
(207Pb/206Pb)0 = 0.7873 ± 0.0032
MSWD = 2.4, p(χ2) = 1e-08
Anchored date = 27.0 ± 1.5 Ma
MSWD = 15
c
NORTHERN FRONT OF THE WHA
expected age = ~59 Ma
date = 35.7 ± 2.8 Ma (n=29)
(207Pb/206Pb)0 = 0.7542 ± 0.0098
MSWD = 1.3, p(χ2) = 0.12
AMZ13
AMZ9
AMZ8
date = 42.9 ± 1.3 Ma (n=65)
(207Pb/206Pb)0 = 0.8130 ± 0.0036
MSWD = 2.3, p(χ2) = 9.1e-09
D-MB4
D-MB3
D-MB2
expected age = ~59 Ma
date = 33.8 ± 1.9 Ma (n=87)
(207Pb/206Pb)0 = 0.750 ± 0.009
MSWD = 2.0, p(χ2) = 1e-07
Anchored date = 49.5 ± 1.4 Ma
MSWD = 7.5
D-TAL3
D-TAL2
D-TAL1
expected age = ~59 Ma
date = 37.3 ± 2.4 Ma (n=106)
(207Pb/206Pb)0 = 0.7880 ± 0.0049
MSWD = 1.7, p(χ2) = 1.9e-5
Anchored date = 55.7 ± 2.3 Ma
MSWD = 5.5
207Pb/206Pb
238U/206Pb

Figure 6

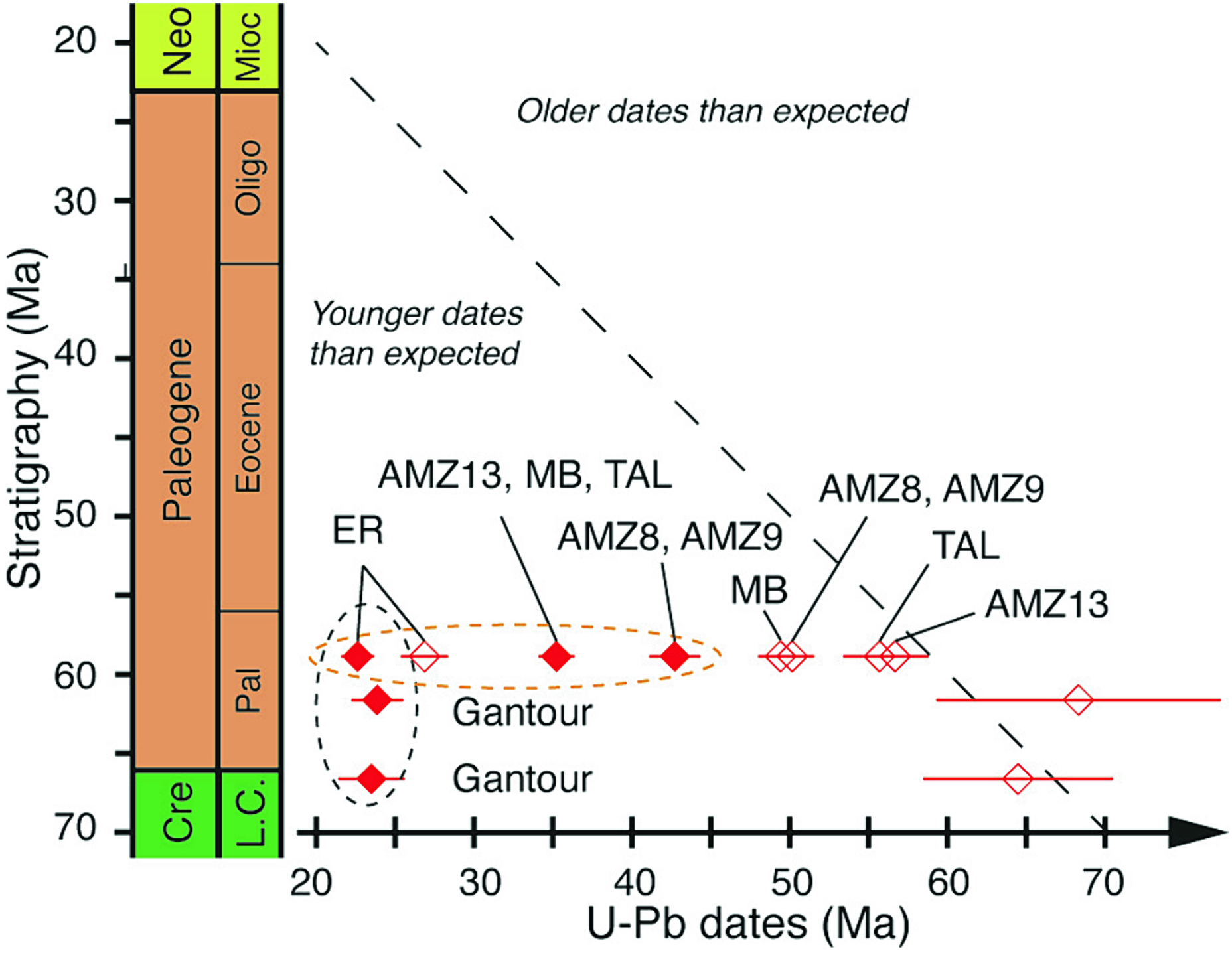
Neo
Mioc
Paleogene
Oligo
Eocene
Pal
Cre
L.C.
20
30
40
50
60
70
Stratigraphy (Ma)
Older dates than expected
Younger dates
than expected
AMZ13, MB, TAL
ER
AMZ8, AMZ9
AMZ8, AMZ9
MB
TAL
AMZ13
Gantour
Gantour
20
30
40
50
60
70
U-Pb dates (Ma)

Figure 7

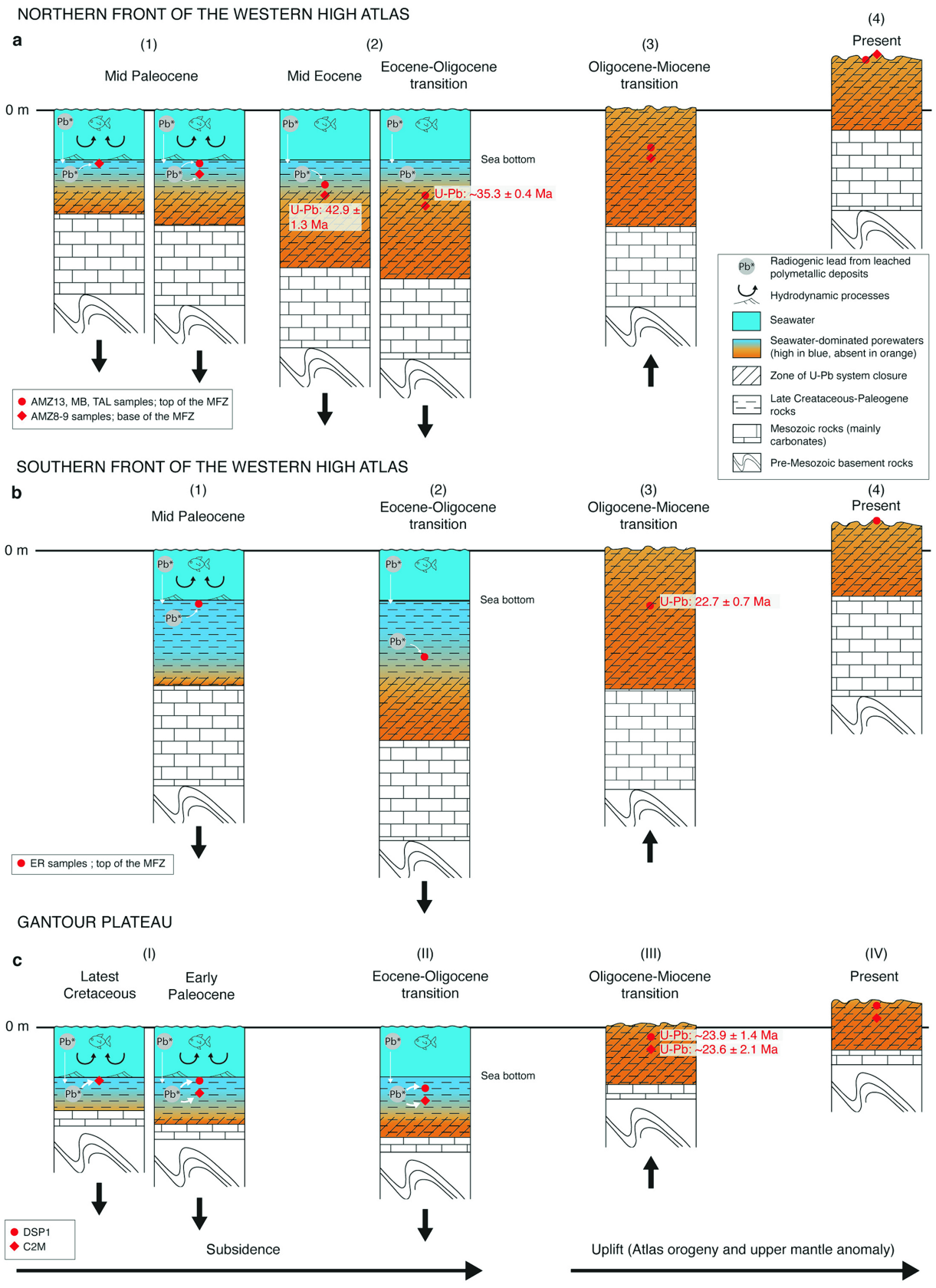
NORTHERN FRONT OF THE WESTERN HIGH ATLAS
a
(1)
Mid Paleocene
(2)
Mid Eocene
Eocene-Oligocene transition
(3)
Oligocene-Miocene transition
(4)
Present
0 m
Sea bottom
U-Pb: 42.9 ± 1.3 Ma
U-Pb: ~35.3 ± 0.4 Ma
AMZ13, MB, TAL samples; top of the MFZ
AMZ8-9 samples; base of the MFZ
Radiogenic lead from leached polymetallic deposits
Hydrodynamic processes
Seawater
Seawater-dominated porewaters (high in blue, absent in orange)
Zone of U-Pb system closure
Late Creataceous-Paleogene rocks
Mesozoic rocks (mainly carbonates)
Pre-Mesozoic basement rocks
SOUTHERN FRONT OF THE WESTERN HIGH ATLAS
b
(1)
Mid Paleocene
(2)
Eocene-Oligocene transition
(3)
Oligocene-Miocene transition
(4)
Present
0 m
Sea bottom
U-Pb: 22.7 ± 0.7 Ma
ER samples ; top of the MFZ
GANTOUR PLATEAU
c
(I)
Latest Cretaceous
Early Paleocene
(II)
Eocene-Oligocene transition
(III)
Oligocene-Miocene transition
(IV)
Present
0 m
Sea bottom
U-Pb: ~23.9 ± 1.4 Ma
U-Pb: ~23.6 ± 2.1 Ma
DSP1
C2M
Subsidence
Uplift (Atlas orogeny and upper mantle anomaly)

Figure 8